Review

Vortex Methods for Flow Simulation

A. LEONARD

Ames Research Center, NASA, Moffett Field, California 94035

Recent progress in the development of vortex methods and their applications to the numerical simulation of incompressible fluid flows are reviewed. Emphasis is on recent results concerning the accuracy of these methods, improvements in computational efficiency, and the development of three-dimensional methods. Simulations of several example flows which display some of the strengths and weaknesses of vortex methods are presented.

1. INTRODUCTION

Many incompressible flows at high Reynolds numbers are characterized by regions of concentrated vorticity imbedded in irrotational fluid. By the theorems of Helmholtz and Kelvin we know that the inviscid motion of the vorticity in these regions is given by the local fluid velocity which in turn is determined kinematically from the vorticity field. Thus, it is mathematically correct and often very convenient to consider inviscid fluid dynamics in terms of parcels of vorticity which induce motion on each other as an alternative to pressure–velocity considerations. By this mutual induction process a vortex ring propels itself along its axis and a pair of aircraft-trailing vortices induce downward motion, each upon the other. Vortex methods simulate flows of this type by discretizing the vorticity-containing regions and tracking this discretization in a Lagrangian reference frame. The required local velocities are computed as the solution to a Poisson equation for the velocity field, often in terms of a Green's function or Biot–Savart integration. Typically, the Lagrangian coordinates of this discretization satisfy a nonlinear system of ordinary differential equations giving the time evolution of the coordinates.

Recent progress in the development of vortex methods with particular emphasis on improvements in accuracy and computational efficiency and on the development of three-dimensional methods and their application is reviewed in this paper. Other recent review articles on vortex methods [1–4] provide excellent background on the historical development of the method and its application to two-dimensional problems, especially the roll-up of a vortex sheet and flow past bluff bodies. This

paper primarily discusses the results and applications that provide insight into the strengths and weaknesses of vortex methods.

The plan of this paper is as follows. In Section 2 the point vortex and vortex blob methods for two-dimensional flows are presented. Several recent results are discussed concerning the numerical analysis of the latter scheme, e.g., the preservation of globally conserved quantities and the analysis of the spatial discretization error resulting from the convection of fixed blobs of vorticity. An application to the two-dimensional mixing layer is briefly described. The contour dynamics method is also discussed in this section. This method is a generalization of the "water-bag" model used to study plasma dynamics and is fairly new in its application to fluid dynamics. The method has therefore not had a long time to mature, but it has a number of interesting features that deserve consideration in this paper.

In Section 3 the simulation of three-dimensional flows with vortex methods is discussed. Here a natural way to represent the vorticity is in the form of closed tubes or filaments of vorticity, although other schemes are under investigation. Applications to aircraft-trailing vortices and to a turbulent spot in a laminar boundary layer are presented. Hybrid schemes that use an Eulerian mesh to solve the Poisson equation for the velocity field are discussed in Section 4. The goal of these schemes is to avoid the high cost of the Biot–Savart integration if many vortex elements are used while enjoying most of the advantages of pure Lagrangian schemes.

2. TWO-DIMENSIONAL SIMULATIONS

A. *Point Vortex Method*

Apparently the first attempt to simulate a flow by a vortex method was by Rosenhead [5], who in 1931 approximated the motion of a two-dimensional vortex sheet by following the movement in time of a system of point vortices. Thus, the vorticity originally concentrated along a line in two dimensions (vortex sheet) was concentrated even further into a finite number of point vortices for simulation purposes. In this point vortex method the scalar vorticity field ω has the representation

$$\omega(\mathbf{x}, t) = \sum_{i=1}^{N} \Gamma_i \delta[\mathbf{x} - \mathbf{x}_i(t)], \tag{1}$$

where δ is the two-dimensional Dirac delta function, $\mathbf{x}_i = (x_i, y_i)$ are the locations of the N vortices, and the Γ_i are their respective circulations. In general, the circulation of region $\mathcal{R}$ is defined by

$$\Gamma_{\mathcal{R}} = \int_{\mathcal{R}} \omega \, d\mathbf{x}. \tag{2}$$

To satisfy the inviscid vorticity transport equation,

$$\frac{\partial \omega}{\partial t} + (\mathbf{u} \cdot \nabla)\omega = 0, \tag{3}$$

or

$$\frac{D\omega}{Dt} = 0, \tag{4}$$

the velocity of each vortex must be given by the value of the velocity field at its present location,

$$\frac{d\mathbf{x}_i}{dt} = \mathbf{u}(\mathbf{x}_i, t). \tag{5}$$

The velocity field is computed as the solution to the Poisson equation

$$\nabla^2 \mathbf{u} = -\nabla \times (\omega \hat{e}_z), \tag{6a}$$

where $\hat{e}_z$ is the unit vector in the z-direction and the boundary condition at a solid surface with unit normal $\mathbf{n}$ is

$$\mathbf{u} \cdot \mathbf{n}\big|_{\text{surface}} = 0. \tag{6b}$$

If the two-dimensional flow field has no interior boundaries and the fluid is at rest at infinity, the solution to (6) may be written as the Biot–Savart integral,

$$\mathbf{u}(\mathbf{x}, t) = -\frac{1}{2\pi} \int \frac{(\mathbf{x} - \mathbf{x}') \times \hat{e}_z \omega(\mathbf{x}', t)\, d\mathbf{x}'}{|\mathbf{x} - \mathbf{x}'|^2}. \tag{7}$$

Using the representation (1) in (7) we find that the $\mathbf{x}_i$ are the solution to the following system of $2N$ nonlinear ODE's:

$$\frac{d\mathbf{x}_i}{dt} = -\frac{1}{2\pi} \sum_{\substack{j=1 \\ j \neq i}}^{N} \frac{(\mathbf{x}_j - \mathbf{x}_j) \times \hat{e}_z \Gamma_j}{|\mathbf{x}_i - \mathbf{x}_j|^2}. \tag{8}$$

Rosenhead's calculations were done by hand. With the advent of computers, further attempts were made to achieve "better" results by following more point vortices with more accurate time integration schemes (see e.g., Birkhoff and Fisher [6]). In many cases the vortices achieved a chaotic state of motion. It now appears that using an increased number of point vortices of decreased strength will not yield a converged solution. Point vortices are simply too singular. (In fact the original problem that Rosenhead attempted to study—the dynamics of a vortex sheet—is ill posed [7] in the sense that nonsmooth solutions will develop in finite time for arbitrarily small initial disturbances.)

Thus, although the point vortex method faithfully solves the Euler (inviscid) equations, a system of point vortices may do a poor job of representing a physically interesting vorticity field. Ironically, best results with the point vortex method often are achieved by using only a few vortices with a diffusive time integration scheme.

B. *Vortex Blob Method*

More recently, many investigators have used vortices with finite cores or vortex blobs in their simulations [8, 9]. The vorticity field is now represented by

$$\omega(\mathbf{x}, t) = \sum_{i=1}^{N} \Gamma_i \gamma_i |\mathbf{x} - \mathbf{x}_i(t)|, \tag{9}$$

where γ_i is the vorticity distribution within the vortex located at $\mathbf{x}_i$ with the normalization

$$\int \gamma_i(\mathbf{x}) \, d\mathbf{x} = 1. \tag{10}$$

We assume that the differences in the distributions between the vortices depend only on a parameter σ_i, i.e., γ_i is given by

$$\gamma_i(\mathbf{x} - \mathbf{x}_i) = (1/\sigma_i^2) \, f(|\mathbf{x} - \mathbf{x}_i|/\sigma_i), \tag{11}$$

where the shape or distribution function f is common to all vortex elements. The quantity σ_i is clearly a measure of the spread or core size of the vortex. For example, the calculation of the dispersion $\langle x^2 \rangle$ defined by

$$\langle x^2 \rangle = \int |\mathbf{x}|^2 \, \gamma_i(\mathbf{x}) \, d\mathbf{x} \tag{12}$$

yields

$$\langle x^2 \rangle = \sigma_i^2 \, 2\pi \int_0^\infty f(y) \, y^3 \, dy. \tag{13}$$

We will refer to σ_i as the core of vortex element i. The velocity induced by the vorticity field (9) is given by

$$\mathbf{u}(\mathbf{x}, t) = -\frac{1}{2\pi} \sum_{j=1}^{N} \frac{(\mathbf{x} - \mathbf{x}_j) \times \hat{e}_z \Gamma_j \, g(|\mathbf{x} - \mathbf{x}_j|/\sigma_j)}{|\mathbf{x} - \mathbf{x}_j|^2}, \tag{14}$$

where g is given by

$$g(y) = 2\pi \int_0^y f(z) z \, dz. \tag{15}$$

Thus, the use of distributed vortex cores or vortex blobs yields more realistic vorticity distributions and bounded induced velocities for all the vortex elements.

A number of core distribution functions have been employed. For example, the Gaussian distribution

$$\gamma(\mathbf{x}) = \frac{1}{\pi \sigma^2} \exp(-|\mathbf{x}|^2/\sigma^2) \tag{16}$$

can be used to satisfy identically the viscous part of the vorticity transport equation for a viscous fluid, i.e., the right-hand side of

$$\frac{D\omega}{Dt} = \nu \nabla^2 \omega, \tag{17}$$

where ν is the kinematic viscosity. To do so requires that σ^2 grow linearly in time as

$$\frac{d\sigma^2}{dt} = 4\nu. \tag{18}$$

Chorin [8] has employed a γ with the behavior

$$\gamma \sim 1/|\mathbf{x}|, \qquad |\mathbf{x}| \to 0, \tag{19}$$

to obtain a constant induced velocity within the core, a property which is of some benefit for boundary-layer simulations. Hald [10] and Leonard [11] have shown that using γ containing both signs of vorticity can increase the spatial order of accuracy. We will return to this point later.

The velocity of these blobs must also be specified. Most studies have used the following, referred to here as scheme A:

$$\frac{d\mathbf{x}_i}{dt} = \mathbf{u}(\mathbf{x}_i, t)$$

$$= -\frac{1}{2\pi} \sum_{j=1}^{N} \frac{(\mathbf{x}_i - \mathbf{x}_j) \times \hat{e}_z \Gamma_j \, g(|\mathbf{x}_i - \mathbf{x}_j|/\sigma_j)}{|\mathbf{x}_i - \mathbf{x}_j|^2}, \tag{20}$$

i.e., the velocity field evaluated at the center of the blob. Also of some merit is the scheme—referred to here as scheme B—using the vorticity-weighted average of the velocity over the blob,

$$\frac{d\mathbf{x}_i}{dt} = \int \gamma_i(\mathbf{x}_i - \mathbf{x}') \, \mathbf{u}(\mathbf{x}', t) \, d\mathbf{x}'$$

$$= -\frac{1}{2\pi} \sum_{j=1}^{N} \frac{(\mathbf{x}_i - \mathbf{x}_j) \times \hat{e}_z \Gamma_j m(|\mathbf{x}_i - \mathbf{x}_j|, \sigma_i, \sigma_j)}{|\mathbf{x}_i - \mathbf{x}_j|^2}, \tag{21}$$

where m is defined by

$$m(|\mathbf{x}_i - \mathbf{x}_j|, \sigma_i, \sigma_j)$$

$$= (2\pi)^2 \int_0^\infty \int_0^\infty xyf(x) f(y) j(|\mathbf{x}_i - \mathbf{x}_j|, \sigma_i x, \sigma_j y) \, dx \, dy$$

and j is given by

$$j(z, s, t) = 1, \qquad\qquad\qquad s + t \leqslant z,$$

$$= \frac{1}{\pi} \cos^{-1}\left(\frac{s^2 + t^2 - z^2}{2st}\right), \qquad |s - t| \leqslant z \leqslant s + t,$$

$$= 0, \qquad\qquad\qquad z \leqslant |s - t|.$$

C. Spatial Accuracy

As mentioned above, the point vortex method, neglecting time integration errors, satisfies the inviscid equations of motion exactly. We now consider the spatial accuracy of the vortex blob technique. In this case error arises because the computational elements are assumed to retain the same shape for all time even though a real fluid element carrying this vorticity may suffer considerable strain, as illustrated in Fig. 1.

One measure of accuracy of a numerical method is its ability to satisfy integral constraints on the fluid motion. In two-dimensional flows at rest at infinity and with no interior boundaries, the following integrals are invariants of the motion, inviscid or viscous:

$$\int \omega \, d\mathbf{x} = \text{const.}, \tag{22}$$

$$\int \mathbf{x} \times \hat{e}_z \omega \, d\mathbf{x} = \text{const.} \tag{23}$$
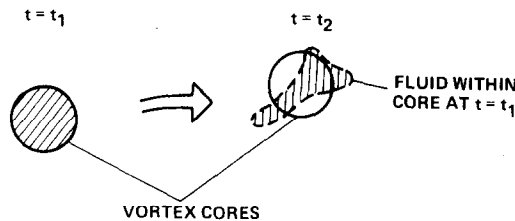

FIG. 1. Schematic showing constancy of shape of a computational element versus distortion of actual fluid element.

Equations (22) and (23) express, respectively, the conservation of total circulation and linear impulse. Three additional constraints for inviscid motion are

$$\int \mathbf{x} \times \mathbf{x} \times \hat{e}_z \omega \, d\mathbf{x} = \text{const.} \tag{24}$$

$$\iint \omega(\mathbf{x}) \, \omega(\mathbf{x}') \log |\mathbf{x} - \mathbf{x}'| \, d\mathbf{x} \, d\mathbf{x}' = \text{const.} \tag{25}$$

$$\int f(\omega) \, d\mathbf{x} = \text{const.} \tag{26}$$

$$(f \text{ arbitrary}),$$

where (24) expresses conservation of angular impulse, (25) is related to the total kinetic energy, and (26) is a consequence of the fact that the vorticity of each fluid particle is constant and the flow is incompressible. It can be shown easily that scheme B satisfies the first three invariants [11]. In general, scheme A will satisfy the first three invariants only if $\sigma_i = \sigma$ for all i. Otherwise the simple modification

$$g(|\mathbf{x}_i - \mathbf{x}_j|/\sigma_j) \to g(|\mathbf{x}_i - \mathbf{x}_j|/((\sigma_i^2 + \sigma_j^2)/2)^{1/2})$$

in Eq (20) for $d\mathbf{x}_i/dt$ will ensure that the three invariants (22) to (24) are satisfied. Only scheme B satisfies the energy invariant. Neither scheme will satisfy (26) in general. The consequences of not satisfying the energy constraint are not known. Usually one is looking for some dissipation anyway so that energy conservation for the convective motion is not vital unless, of course, a numerical instability results.

Hald and Del Prete [12] studied the convergence of the vortex blob method to the solution of the Euler equations. They were able to show convergence but for only a limited time interval with an error that grows exponentially in time. Later Hald [10] found an improved proof of convergence in which the error remains independent of time. We will return to Hald's results after a brief discussion of the local spatial truncation error of the method.

The vortex blob method as described above is equivalent to approximating the convective derivative by

$$(\mathbf{u} \cdot \nabla)\omega = \nabla \cdot (\mathbf{u}\omega) \approx \nabla \cdot \left[\sum_{i=1}^{N} \Gamma_i \gamma_i (\mathbf{x} - \mathbf{x}_i) \frac{d\mathbf{x}_i}{dt} \right]. \tag{27}$$

This may be verified by noting that the right-hand side of (27) is equal to $-\partial\omega/\partial t$ with ω given by (9). Therefore, the local truncation error $\varepsilon(\mathbf{x})$ is the difference of the two terms or

$$\varepsilon(\mathbf{x}) = \nabla \cdot \left[\sum_{i=1}^{N} \Gamma_i \gamma_i (\mathbf{x} - \mathbf{x}_i) \left(\mathbf{u}(\mathbf{x}) - \frac{d\mathbf{x}_i}{dt} \right) \right] \tag{28}$$

A Taylor series expansion of $\mathbf{u}(\mathbf{x}_i)$ about $\mathbf{x}$ yields, for scheme A,

$$\mathbf{u}(\mathbf{x}) - \frac{d\mathbf{x}_i}{dt} = \mathbf{u}(\mathbf{x}) - \mathbf{u}(\mathbf{x}_i),$$

$$= [(\mathbf{x} - \mathbf{x}_i) \cdot \nabla] \mathbf{u}(\mathbf{x}) + \cdots,$$

(29)

so that

$$\varepsilon(\mathbf{x}) \approx \nabla \cdot \left\{ \sum_{i=1}^{N} \Gamma_i \gamma_i (\mathbf{x} - \mathbf{x}_i) [(\mathbf{x} - \mathbf{x}_i) \cdot \nabla] \mathbf{u}(\mathbf{x}) \right\}.$$

(30)

In many cases of interest the quantity $(\mathbf{x} - \mathbf{x}_i) \gamma_i$ can be related to derivatives of γ_i. For a Gaussian core, for example,

$$(\mathbf{x} - \mathbf{x}_i) \gamma_i = (\sigma_i^2/2) \nabla \gamma_i (\mathbf{x} - \mathbf{x}_i).$$

(31)

Thus,

$$\varepsilon(\mathbf{x}) \approx \nabla \cdot \left[\sum_{i=1}^{N} \Gamma_i (\sigma_i^2/2)(\nabla \gamma_i \cdot \nabla)\mathbf{u} \right],$$

(32)

i.e., the vortex method using Gaussian cores is second order accurate in σ. Because smooth distributions in vorticity can be achieved by choosing $\beta \sim \sigma$, where β is the average spacing between blobs, the method is also second order in β. The same result applies to scheme B following a slightly more involved analysis. If $\sigma_i = \sigma$ for all i, we can write (32) as

$$\varepsilon(\mathbf{x}) \approx \frac{\sigma^2}{2} S_{jk} \frac{\partial^2 \omega}{\partial x_j \partial x_k},$$

(33)

where repeated indices are summed and S_{jk} is the strain rate tensor

$$S_{jk} = \frac{1}{2} \left(\frac{\partial u_j}{\partial x_k} + \frac{\partial u_k}{\partial x_j} \right).$$

For incompressible flow S_{jk} has one real positive and one real negative eigenvalue of equal magnitude. Thus, the error is not diffusive to order σ^2.

Higher order schemes can be generated easily by choosing γ to depend only on the magnitude of its argument and demanding, for example, that

$$\mathbf{x}\gamma(\mathbf{x}) = (-1)^{m/2} \frac{(\sigma/2)^m}{m} \nabla(\nabla^{m-2}) \gamma(\mathbf{x})$$

(34)

for even integers m, yielding an mth order scheme. The form of the resulting γ can be determined by Fourier transformation of (34). If

$$\hat{\gamma}(\mathbf{k}) = \int e^{-i\mathbf{k} \cdot \mathbf{x}} \gamma(\mathbf{x}) \, d\mathbf{x}, \tag{35}$$

we find

$$\hat{\gamma}(\mathbf{k}) = e^{-(k\sigma/2)^m}, \tag{36}$$

and hence

$$\gamma(\mathbf{x}) = \frac{1}{2\pi} \int_0^\infty e^{-(k\sigma/2)^m} J_0(k \, |\mathbf{x}|) k \, dk. \tag{37}$$

As $m \to \infty$ we obtain a spectral-like scheme with

$$\gamma(\mathbf{x}) = \frac{1}{2\pi |\mathbf{x}| \sigma} J_1 \left(\frac{2 |\mathbf{x}|}{\sigma} \right). \tag{38}$$

The core distributions for $m = 2$, 4, and ∞ are shown in Fig. 2. It would be interesting to test some of these higher order schemes. Many more possibilities exist for a given order. The choice of (34) is only a particular one. A general class of core distributions for mth order schemes has Fourier transforms with the property

$$\hat{\gamma}(k) = 1 - O(k^m), \qquad k \to 0,$$

corresponding to the following $(m - 2)/2$ integral constraints on the core distribution function,

$$\int \gamma(\mathbf{x}) |\mathbf{x}|^{2j} \, d\mathbf{x} = 0, \qquad j = 1, 2, \ldots, \frac{m - 2}{2}.$$
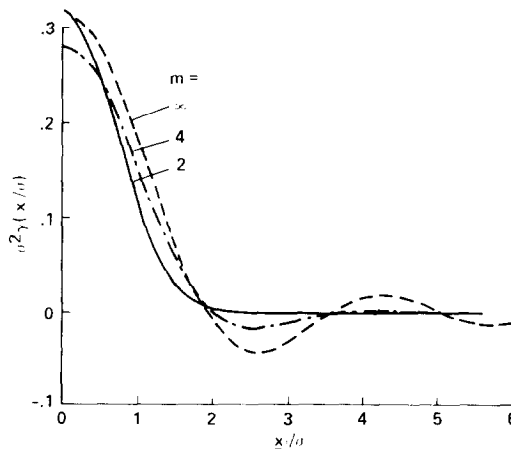

FIG. 2.   Vortex core distributions for $m = 2$, 4, and ∞.

Hald and Del Prete [12] were first to determine that specially constructed core distributions could be used to achieve higher order accuracy and they performed numerical experiments to verify their analysis. The system of constraints given above for an mth order scheme represents the generalization of their single constraint for the case $m = 4$. Hald [10] used distribution functions satisfying the $m = 4$ constraint to construct his convergence proof. His analysis is quite involved, apparently because he desires a given order of accuracy after an arbitrary time of integration. According to Hald, one should use relatively large cores sized by $\sigma \sim \beta^{1/2}$ rather then β. Thus, a fourth order scheme $(m = 4)$ becomes only second order in β. Further work is required to better understand the meaning of this requirement. It may be related to the fact that a shear layer, for example, may experience continued stretching along part of its length, thinning out of vortex blobs representing that portion of the layer. To maintain high accuracy in approximating a continuum of vorticity one would have to start with a high degree of overlapping of the vortex cores.

D. Viscous Effects

The appearance of the vorticity diffusion term $\nu \nabla^2 \omega$ in the vorticity transport equation has two ramifications: vorticity creation at the boundary and diffusion of vorticity in the flow field. As mentioned above the diffusion of vorticity can be accounted for accurately by allowing Guassian vortex cores to increase in size according to (18). An alternative scheme of adding a random walk each time step was introduced by Chorin [8]. Here the step length is propertional to $(\nu \Delta t)^{1/2}$. The idea is that the effects of viscosity are correctly reproduced in a statistical sense. Ashurst [13] has tested the random walk schemes on a time-developing boundary layer and achieved satisfactory results. Milinazzo and Saffman [14] found that to achieve accurate results for the viscous decay of a uniform vortex using a random walk scheme the number of vortex elements had to be large compared to the Reynolds number. (see however [15, 16]). Other techniques used in the simulation may result in the diffusion of vorticity whether it is intentional or not. Two examples are the combining of vortex blobs and the use of low order time integration schemes.

In flows where boundary-layer separation is an inportant physical phenomenon, such as flow past bluff bodies, the vorticity creation process at solid wall boundaries and the subsequent transport of vorticity along the boundary must be modeled correctly. Many authors introduce circulation at or near the separation points, relying on boundary-layer calculations, experimental information, or other a priori knowledge to determine the separation points [1, 17, 18]. The rate of creation of vortices at each point is determined from the kinematic condition,

$$\frac{d\Gamma}{dt} = -\frac{1}{2}(u_+^2 - u_-^2), \tag{39}$$

where $u_\pm$ are the upper and lower speeds on either side of the separating shear layer and $d\Gamma/dt$ is the flow of circulation in the shear layer passing a fixed station, as indicated in Fig. 3. If relatively few vortices are used per unit length to represent the free shear layer, care must be taken to avoid spurious results. Various rules have been
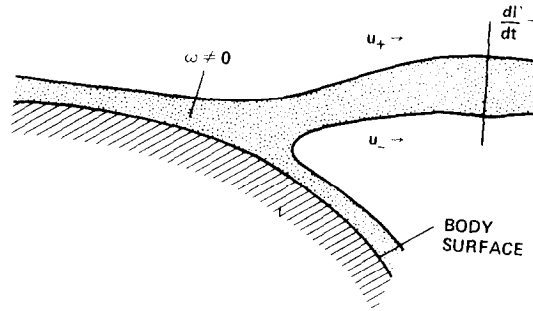
FIG. 3. Schematic of separating boundary layer.

developed to choose the point of creation relative to the body surface and other parameters of the creation process [1, 17, 18].

A more ambitious approach is to create vortices at the boundary to maintain the no-slip condition at the surface (see Fig. 4). The vortices thus created that are still close to the surface represent the boundary layer. If the mechanics of the boundary layer are being simulated correctly, vortices will separate automatically from the surface layer near the true separation points. A numerical method based on these notions is as follows [8]. At each time step,

1. Create vortices at the boundary to maintain the no-slip condition at the surface.

2. Move vortices with the local velocity to satisfy the inviscid part of the equations of motion, using image vorticity or boundary integral methods to satisfy the tangency boundary condition (6b).

3. Simulate vorticity diffusion by a change in core size or a random walk.

Such a split scheme was shown by Chorin *et al.* [19] to converge to the solution to the Navier–Stokes equaions as long as each substep is convergent.

To achieve an accurate simulation of high Reynolds number, boundary-layer flows one would like the vortex core size to be some fraction, f, of the boundary-layer
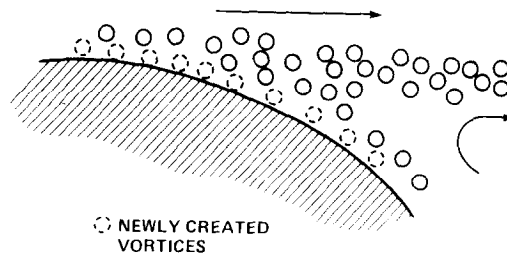

FIG. 4. Vortex creation to satisfy the no-slip condition.

thickness, δ, or $\sigma \sim f\delta$, and to have the boundary layer, of streamwise extent L, filled with vortex blobs. The number of blobs N required to represent the boundary layer is then given by

$$N\sigma^2 \sim \delta L,$$

(40)

or

$$N \sim \frac{L}{\delta f^2} \sim \frac{Re^{1/2}}{f^2}.$$

(41)

For example, to simulate flow past a cylinder at $Re = 10,000$ would require approximately 5000 vortex blobs to represent the boundary layer, assuming the layer averages 5 to 10 blobs in thickness. Because the operation count is $O(N^2)$/time step, computer budgets to date have not allowed such extravagance. One has been forced to rely on free parameters in the vortex creation process to obtain good results. One parameter, for example, is the distance of the creation point to the surface representing the initial diffusion of vorticity away from the wall. Nevertheless, the choice of these parameters often can be made on a sound physical basis, and the results have been very encouraging [8, 20, 21].

Another approach is to take a lesson from the boundary-layer approximation: derivatives along the direction tangent to the surface are much smaller than derivatives in the normal direction. In Eulerian methods, use of a high-aspect-ration grid cell is standard practice near a solid boundary. For vortex methods, boundary-layer theory suggests using vortex blobs that are elongated in the tangent direction, thus requiring fewer blobs to represent the boundary layer. Chorin [22] made a specific suggestion in this direction. He proposed the use of finite vortex sheets in the vicinity of the boundary. Cheer [23] has applied this method to the problem of flow past a cylinder for $Re = 1000$. Using 100–200 vortex sheets to represent the boundary layer and 500–1000 blobs for the wake, she obtained a drag coefficient that is within 2 % of experiment. The lift history fluctuated about zero but the data were not analyzed to obtain a Strouhal frequency.

E. *Applications of the Blob Method*

To illustrate some of the ideas put forth above, an example flow was simulated by P. Spalart (Stanford University, Stanford, Calif.) using a vortex blob method. The flow is a mixing layer shown schematically in Fig. 5; see Ashurst [13] for a more thorough study of this flow using vortex methods. Acton [24] has studied the time-developing mixing layer (with spatial periodicity).

At every time step, a new vortex with a Gaussian core is placed at the left-hand boundary at $y = 0$. The circulation Γ of every vortex is given by

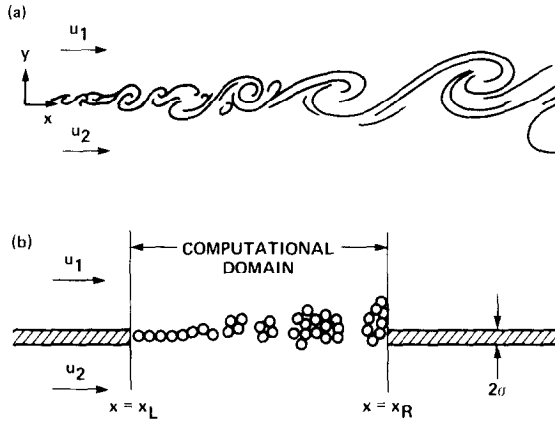$$\Gamma = -\frac{\Delta t}{2}(u_1^2 - u_2^2),$$

(42)

FIG. 5.   Schematic of (a) two-dimensional mixing layer and (b) vortex simulation of the mixing layer.

in satisfaction of Eq. (39). Since the vortices move with speed $(u_1 + u_2)/2$ in an undisturbed shear layer, the nominal spacing between vortices d is

$$d = \frac{2\,\Delta t}{u_1 + u_2}. \tag{43}$$

The core size σ must be comparable to d to obtain a smooth representation of the shear layer. In this simulation

$$\sigma = 3d. \tag{44}$$

The inflow condition for vorticity at the left boundary is satisfied by the creation process cited above. The outflow condition is satisfied simply by removing a vortex from the computation as it passes the right boundary at $x = x_R$. This assumes that there is negligible transport of vorticity in the negative x direction at $x = x_R$. The velocity field must also be computed at every time step, and contributions to the velocity from vorticity outside the computational domain plus the maen flow $(u_1 + u_2)/2$, must be included. The additional vorticity is assumed to be in the form of two semi-infinite sheets of thickness 2σ spanning

$$-\infty \leqslant x \leqslant x_L - d$$

and

$$x_R \leqslant x \leqslant \infty,$$

with circulation/unit length equal to $u_1 - u_2$. The sheet downstream of $x = x_R$ is clearly only an approximation to the actual unsteady shear layer that would exist in
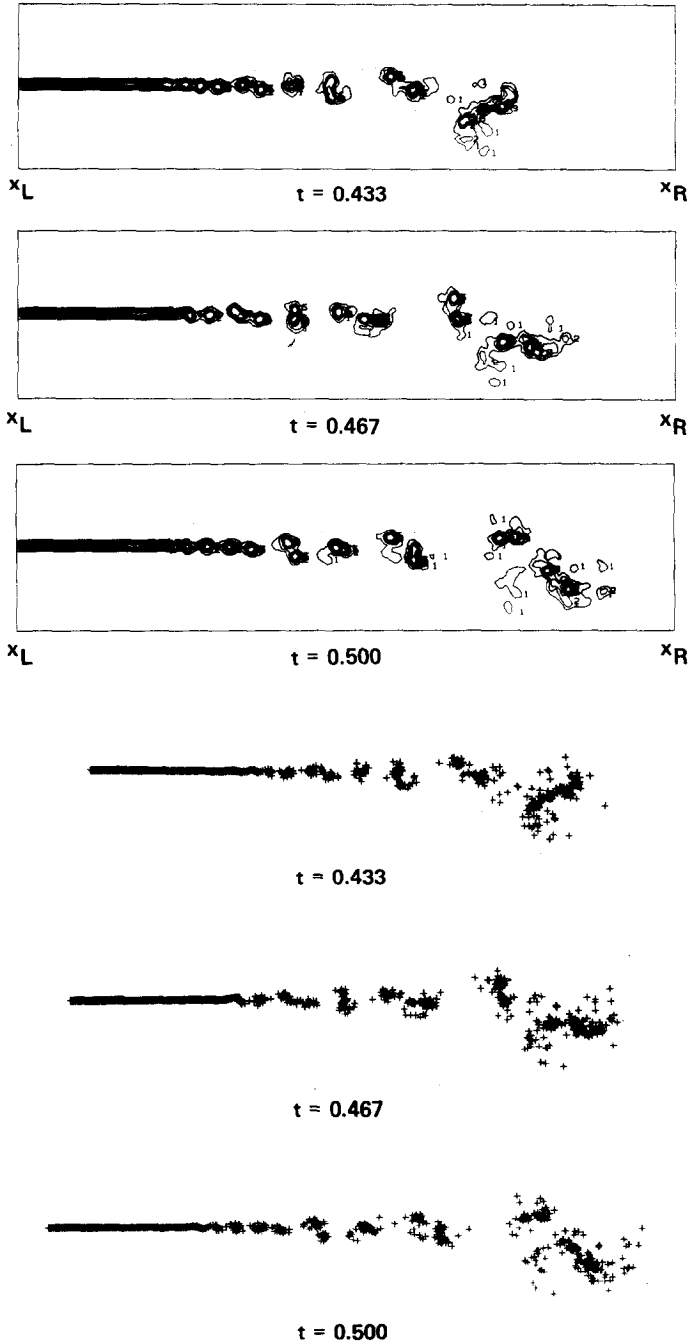
FIG. 6. Vorticity contour plots and corresponding vortex locations in the two-dimensional mixing layer. $u_1 = 3$, $u_2 = 1$, $x_R - x_1 = 1$, $\sigma = 0.005$; contour levels, -25, -75, -125, -175,....

this region. A slight improvement might be to use a thickened shear layer for $x \geqslant x_R$. Another alternative would be to follow the vortex blobs farther downstream but to combine vortices that are close to each other in the downstream portion of the computational domain. This procedure seems analogous to using a coarse downstream grid in an Eulerian calculation.

$\Delta UL/\nu = 250$ $\Delta UL/\nu = 1000$
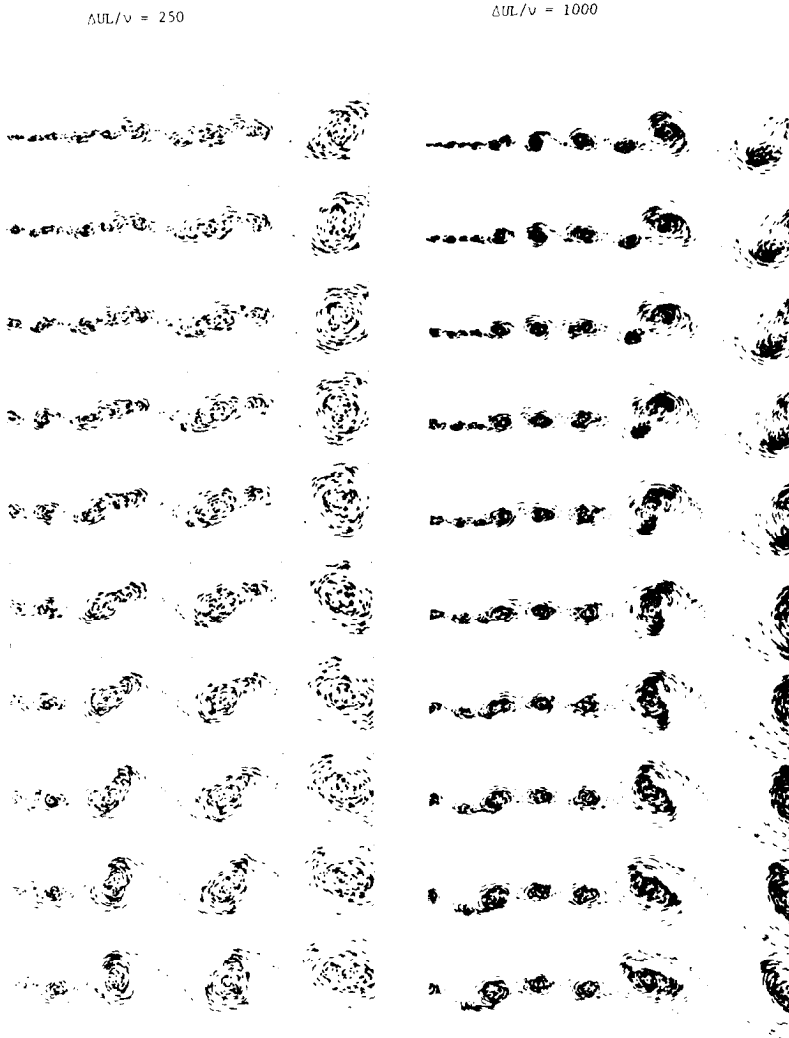
FIG. 7. Streakline plots of each discrete vortex for a unit time $(L/\Delta U)$ with respect to the average velocity. The field of view is equal to $40L$. The top plots have the origin at the left with each succeeding plot displaced two units downstream and two units later in time. Left column is $250\ Re$ flow and right column is $1000\ Re$; $(u_1 + u_2)/(2\ \Delta u) = 1.05$. (Permission to use figure granted by W. T. Ashurst.)

The start-up procedure consists of moving the upstream edge of the downstream vortex sheet with constant speed $(u_1 + u_2)/2$ from $x = x_L$ to its permanent location at $x = x_R$. This procedure preserves approximately the total circulation in the computational domain and produces only a small perturbation in the shear layer at $x = x_L$ at $t = 0$.

The vortex locations at three instants in time and corresponding vorticity contour plots are shown in Fig. 6. The contour plots demonstrate that a collection of vortex blobs is capable of representing physically reasonable distributions in vorticity. After the start-up phase, the average number of blobs in the computational domain is 600. On the other hand, it is estimated that a mesh of $\approx 22{,}500$ points (300×75) would be required for an Eulerian simulation of this flow with $\Delta x = \Delta y = 2d$. The CPU-time/time-step required on the CDC 7600 is approximately $(N/600)^2$ sec, where N is the number of vortex blobs; the high cost of this method as N increases is obvious.

The time marching algorithm was scheme A with a multistep predictor–corrector integration method. The time step Δt was $\approx 2d/|\mathbf{u}|_{\max}$, demonstrating that rather large time steps can be employed. Vortex methods are not subject to the usual convective instability.

In Ashurst's vortex simulation of the mixing layer [13], several thousand vortex blobs were used to represent the space-developing mixing layer. In Fig. 7, streakline plots produced by displacements of the vortex elements are shown for two Reynolds numbers at 10 succeeding times. The field of view is moving with the average velocity. In this case the higher speed flow is on the bottom. The eddy-pairing process, known to be present in experiments, is clearly shown. In comparing with experiment at moderate Reynolds number, Ashurst found good agreement in mixing layer growth using the random walk technique to simulate viscous diffusion. By adding the viscous growth of the core according to Eqs. (16)–(18) he also obtained very good agreement with turbulent shear stress profile and the longitudinal and normal velocity fluctuation profiles. Good agreement was also obtained at high Reynolds number except for the normal velocity fluctuations. Presumably the presence of streamwise vortices in experimental high Reynolds number flows produces significant effects that are not easily modeled in two-dimensional vortex simulations.

F. *Method of Contour Dynamics*

If the two-dimensional vorticity field is assumed to be initially regionwise constant then, for inviscid motion, it will remain so, each region distorting under the straining action of the velocity field. In this case only the boundaries of each region need be tracked. A numerical scheme based on this observation has been proposed by Zabusky *et al.* [25]; they call it the "method of contour dynamics."

The velocity field required to move the boundary curves reduces to a line integral along these curves (see Fig. 8),

$$\mathbf{u}(\mathbf{x}) = \frac{1}{2\pi} \int_C \Delta\omega \log |\mathbf{x} - \mathbf{r}(\xi', t)| \frac{\partial \mathbf{r}(\xi', t)}{\partial \xi'} \, d\xi', \tag{45}$$
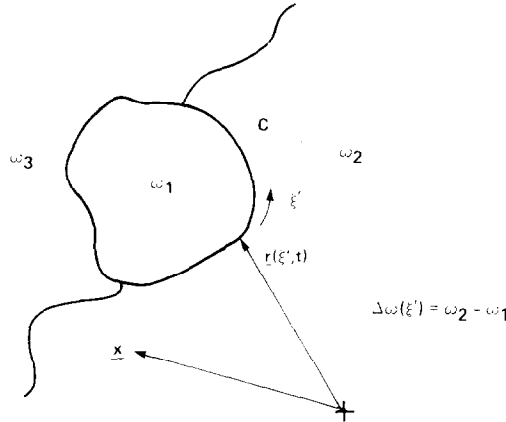
FIG. 8.   Schematic of the integration scheme for the contour dynamics method.

where $\Delta\omega$ is the jump in ω at $\mathbf{r}(\xi', t)$, $\Delta\omega = \omega_{\text{right}} - \omega_{\text{left}}$. The equations of fluid motion then reduce to nonlinear evolution equations for the planar curves representing the region boundaries,

$$\frac{\partial \mathbf{r}(\xi, t)}{\partial t} = \frac{1}{2\pi} \int_C \Delta\omega \, \log |\mathbf{r}(\xi, t) - \mathbf{r}(\xi', t)| \, \frac{\partial \mathbf{r}(\xi', t)}{\partial \xi'} \, d\xi', \qquad (46)$$

where ξ is a material marker along the curve. The only error in computing the evolution of the flow is that made in tracking the motion of these planar curves. For numerical purposes, Zabusky *et al.* mark the curves with node points and follow the points using a straightline approximation to evaluate the integral along each segment of the curve. The motion of such curves with a log singularity in the integrand should be much more favorable to numerical schemes than the motion of vortex sheets with their $1/x$ singularity.

An interesting application of the method has been to determine stationary states of finite-area, constant-vorticity regions, the simplest example being the Kirchoff elliptical vortices, having twofold symmetry. Deem and Zabusky [26] computed families of vortices having threefold and fourfold symmetry, as illustrated in Fig. 9. (In a related calculation in axisymmetric geometry, Norbury [27] determined a family of stationary cross-sectional shapes of vortex rings. In this case $r\omega(r) = $ const. within the vortex ring.)

Examples of flows were also computed where the boundary curves formed singularities, cusps, or filaments. In this situation and in the general case where the total length of the boundary curves would be expected to increase with time, remeshing of the boundary curves will be necessary. In this process, certain fine-scale details will be lost from the simulation. It is hoped, however, that the fine-scale structures that are removed by the remeshing process will have little influence on the
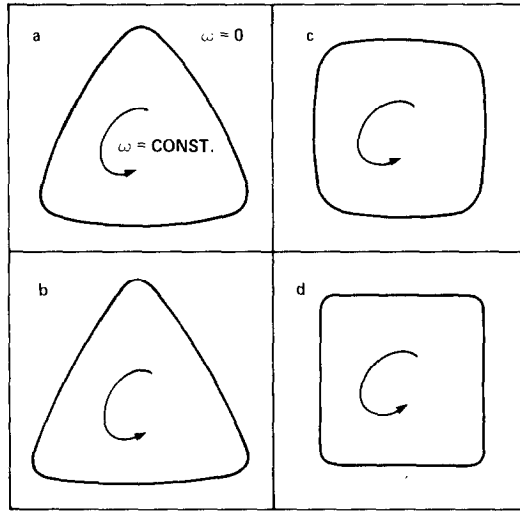
FIG. 9. Threefold (a, b) and fourfold (c, d) symmetry states as computed by the contour dynamics method |26|.

dynamics of the larger scales. It seems that the proper way to view this procedure is to consider the generation of fine scales and their subsequent removal by remeshing as a representation of the turbulent cascade of energy to small scales.

3. THREE-DIMENSIONAL SIMULATIONS

A. Vortex Filaments

A natural generalization to three dimensions of the two-dimensional vortex blob method described in the previous section is to assume that the vorticity field is represented by a collection of L tubes or filaments of vorticity. By Kelvin's theorem the circulation of filament i given by

$$\Gamma_i = \int_{\text{core } i} \boldsymbol{\omega} \cdot d\mathbf{A} \tag{47}$$

is constant in time for an inviscid fluid. The spatial configuration of this filament at time t is given by the space curve $\mathbf{r}_i(\xi, t)$, where ξ is a parameter along the curve, usually a fluid particle marker. Thus, in analogy with the two-dimensional vortex blob method, the vorticity field in three-dimensions is given by

$$\boldsymbol{\omega}(x, t) = \sum_{i=1}^{L} \Gamma_i \int \gamma_i [\mathbf{x} - \mathbf{r}_i(\xi', t)] \frac{\partial \mathbf{r}_i}{\partial \xi'} d\xi', \tag{48}$$

It is assumed that γ_i has the form

$$\gamma_i(\mathbf{x} - \mathbf{r}_i) = \frac{1}{\sigma_i^3}\, p\left(\frac{|\mathbf{x} - \mathbf{r}_i|}{\sigma_i}\right). \tag{50}$$

The quantity σ_i will be referred to as the core radius of filament i. A schematic representation of a vortex filament is shown in Fig. 10.

The resultant velocity is given by the solution to

$$\nabla^2 \mathbf{u} = -\nabla \times \boldsymbol{\omega}, \tag{51a}$$

with the boundary condition,

$$\mathbf{u} \cdot \mathbf{n}\big|_{\text{surface}} = 0. \tag{51b}$$

Using the infinite-medium Green's function for the Poisson equation we find $\mathbf{u}$ in terms of the Biot–Savart integral

$$\mathbf{u}(\mathbf{x}, t) = -\frac{1}{4\pi} \int \frac{(\mathbf{x} - \mathbf{x}') \times \boldsymbol{\omega}(\mathbf{x}', t)\, d\mathbf{x}'}{|\mathbf{x} - \mathbf{x}'|^3} + \nabla\phi, \tag{52}$$

where ϕ is a velocity potential constructed to satisfy the inviscid boundary condition. Inserting the representation (48) into (52) we find that the Biot–Savart integral reduces to a sum of line integrals over each of the space curves representing the vortex filaments,

$$\mathbf{u}(\mathbf{x}, t) = -\frac{1}{4\pi} \sum_{j=1}^{L} \Gamma_j \int \frac{[\mathbf{x} - \mathbf{r}_j(\xi', t)] \times (\partial \mathbf{r}_j/\partial \xi')\, q(|\mathbf{x} - \mathbf{r}_j|/\sigma_j)\, d\xi'}{|\mathbf{x} - \mathbf{r}_j|^3}, \tag{53}$$
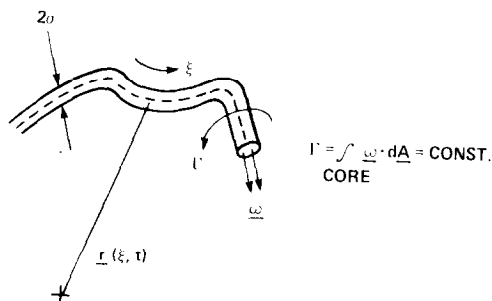

FIG. 10.   Representation of a vortex filament.

where q is defined by

$$q(y) = 4\pi \int_0^y p(t)\, t^2\, dt, \tag{54}$$

and where it is assumed that y_i is spherically symmetric and that no boundaries are present. From the normalization of y_i it is noted that $q(y) \to 1$ as $y \to \infty$ so that at a distance large compared to the core radius the induced velocity may be calculated as if all the circulation were concentrated on the line $\mathbf{r}_i(\xi, t)$. Assuming $p(t) < \infty$, q is $O(y^3)$ for small y; therefore $\mathbf{u}(\mathbf{x}, t)$ remains bounded.

B. *Inviscid Dynamics of* $\mathbf{r}_i, \sigma_i$

In an exact simulation of inviscid flow, vortex lines would move as material lines (Helmholtz' theorem), i.e., with the local velocity. However, in the approximation (48) a collection of vortex lines must be moved as a single entity. Therefore, an appropriately averaged velocity must be chosen. A general form, used in several studies, is

$$\frac{\partial \mathbf{r}_i(\xi, t)}{\partial t} = -\frac{1}{4\pi} \sum_{j=1}^{L} \Gamma_j \int \frac{(\mathbf{r}_i - \mathbf{r}_j) \times (\partial \mathbf{r}_j / \partial \xi')\, s(|\mathbf{r}_i - \mathbf{r}_j|, \sigma_i, \sigma_j)\, d\xi'}{|r_i - r_j|^3}, \tag{55}$$

where s is symmetric in σ_i and σ_j and has properties similar to q,

$$s(y, \sigma_i, \sigma_j) \to 1, \qquad y \to \infty;$$

$$s(y, \sigma_i, \sigma_j) \to O(y^3), \qquad y \to 0.$$

If $s \equiv 1$ we recover the dynamics of a line filament leading to logarithmic singularities for the velocity as discussed below. Therefore, the function s is a mollifier and a necessary ingredient in three-dimensional simulations. The symmetry of s in σ_i and σ_j leads to exact conservation of linear and angular momentum. In addition to a specific choice of s, the dynamics of the core must be chosen. Below are given two particular choices and motivation for each.

In scheme C, s is of the form

$$s = s[|\mathbf{r}_i - \mathbf{r}_j| / ((\sigma_i^2 + \sigma_j^2)/2)^{1/2}] \tag{56a}$$

and satisfies the integral constraint,

$$\int_0^\infty \frac{s(y)}{y}\, dy = \log 4 - \frac{1}{2} + \int_0^1 \frac{\Gamma^2(t)\, dt}{t} + \int_1^\infty \frac{\Gamma^2(t) - 1}{t}\, dt, \tag{56b}$$

where $\Gamma(t)$ is the fraction of circulation within a dimensionless distance $t = r/\sigma$ of the center of the core, given by

$$\Gamma(t) = \left[1 - 4\pi \int_t^\infty p(s)\, s^2 \left(1 - \frac{t^2}{s^2} \right)^{1/2} ds \right]. \tag{56c}$$

For scheme C the dynamics of the core is given by

$$\frac{d}{dt}(\sigma_i^2 \mathscr{L}_i) = 0, \tag{57}$$

where $\mathscr{L}_i(t)$ is the instantaneous total length of filament i,

$$\mathscr{L}_i = \int \left| \frac{\partial \mathbf{r}_i}{\partial \xi} \right| d\xi. \tag{58}$$

In this scheme the integral constraint (56b) ensures that the inviscid dynamics of an arbitrary vortex tube is recovered when the core radius is much smaller than any radius of curvature along the tube [11, 28, 29]. The dynamics of σ_i given by (57) expresses conservation of volume for each filament and produces an increased amplitude of the vorticity within a filament as $\mathscr{L}_i$ increases (vortex stretching). The assumption that σ_i remains independent of position along the filament is suggested by Moore and Saffman [29], who argue that internal waves within the filament would act to smooth any variations along the length of the filament. Equation (57) for σ_i together with the constraint on s, (56b), yields conservation of energy for an arbitrary collection of filaments when the cores have negligible overlap [11]. A specific choice for s [30, 31] is

$$s(y, \sigma_i, \sigma_j) = \frac{1}{[1 + \alpha(\sigma_i^2 + \sigma_j^2)/2y^2]^{3/2}}, \tag{59}$$

where the choice $\alpha = 0.413$ for a Gaussian distribution of vorticity within the core satisfies the integral constraint (56b). Thus, for example, using (55) with (59) one would compute the correct speed of a single vortex ring with a core radius that is small compared to the ring radius [32].

In scheme D we assume, in analogy with scheme B for two dimensions, that the velocity of the space curve is computed as an average over the filament, using the distribution function γ_i as a kernel for the averaging process. Thus,

$$\frac{\partial \mathbf{r}_i}{\partial t} = \int \gamma_i(\mathbf{r}_i - \mathbf{x}') \mathbf{u}(\mathbf{x}', t) \, d\mathbf{x}', \tag{60}$$

giving s in terms of p as

$$s(y, \sigma_i, \sigma_j) = (4\pi)^2 \int_0^\infty \int_0^\infty u^2 v^2 p(u) p(v) h(y, \sigma_i u, \sigma_j v) \, du \, dv, \tag{61a}$$

where

$$\begin{aligned} h(y, w, z) &= 1, & w + z \leqslant y, \\ &= \frac{y^2 - (w - z)^2}{4wzy}, & |w - z| \leqslant y \leqslant w + z, \\ &= 0, & y \leqslant |w - z|. \end{aligned} \tag{61b}$$

Again, the symmetrical appearance of σ_i and σ_j ensures exact conservation of linear and angular momentum. This scheme yields exact conservation of kinetic energy, irrespective of core overlap, if the dynamics of each core is given by

$$\frac{d\sigma_i^2}{dt} = 0. \tag{62}$$

It would seem that (62) violates conservation of volume for the fluid containing vorticity in inviscid motion. In this scheme, however, it is appropriate to think in terms of a "swarm" of filaments with overlapping cores as representing a region of rotational fluid. Then, for example, the local elongation of the filaments defining a physical tube of vorticity as shown in Fig. 11 would lead to a closer packing (and hence greater overlapping of the cores) because of the incompressibility of the fluid. Thus, we obtain approximate conservation of volume of the physical tube of vorticity as well as intensification of the vorticity field within its core because

$$\frac{\partial u_s}{\partial s} > 0 \Rightarrow \frac{\partial u_\xi}{\partial \xi} + \frac{\partial u_\eta}{\partial \eta} < 0,$$

where the nomenclature is defined in Fig. 11.

Based on the above considerations it would seem that scheme C is better suited for the case in which a computational filament is used to represent an actual tube of vorticity and that scheme D should be used to simulate the motion of a distributed continuum of vorticity.

C. Local Induction Approximation

It should be noted that the analog to the two-dimensional point vortex method does not lead directly to an interesting computational technique in three dimensions. If
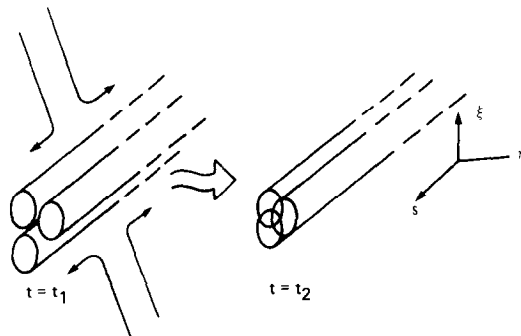

FIG. 11. Schematic of vorticity intensification in the constant-core model.

$\sigma \to 0$, then $s \to 1$ and the leading term for the filament velocity is the self-induced contribution due to the local curvature of the filament,

$$\frac{\partial \mathbf{r}_i}{\partial t} = \frac{\Gamma_i \mathbf{b}}{4\pi\rho_c} \log \frac{\rho_c}{\sigma} + O(1), \tag{63}$$

where ρ_c is the local radius of curvature of the filament and $\mathbf{b}$ is the unit binormal (see Fig. 12). Therefore, a log singularity in the velocity of the filament arises as $\sigma \to 0$. However, using only the leading term for $\partial \mathbf{r}_i/\partial t$ in (63) and assuming that the log term is constant over the filament, one obtains the local induction approximation for the motion of a vortex filament,

$$\frac{\partial \mathbf{r}_i}{\partial t} = C \frac{\partial \mathbf{r}_i}{\partial \xi} \times \frac{\partial^2 \mathbf{r}_i}{\partial \xi^2}, \tag{64}$$

where ξ is now an arc length parameter. Although this approximation is only of theoretical interest, Betchov [33] found analytically a number of interesting properties of the dynamics of space curves governed by (64), including dispersive and diffusive behavior. Later, Hasimoto [34] showed that this dynamics allowed the existence of solitions, nonlinear solitary waves that preserve their identity even after a collision of two waves.

It is interesting to note that there seems to be no analog of the contour dynamics methods for general three-dimensional flows. What would be required is that the support of $\nabla \times \boldsymbol{\omega}$ remain on two-dimensional surfaces moving with the fluid velocity. Unfortunately, the transport equation for $\nabla \times \boldsymbol{\omega}$ contains source terms in a three-dimensional flow while it does not in two-dimensions.
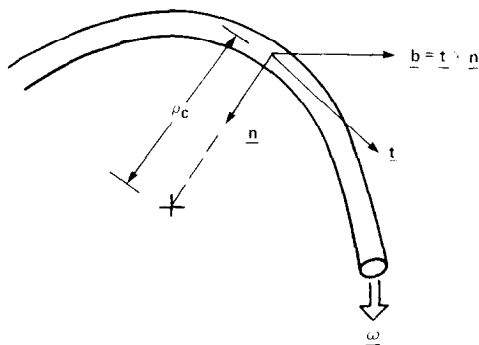

FIG. 12.   Definition of terms for the local induction approximation.

D. *Viscous/Subgrid-Scale Effects*

As in two-dimensions, the effect of the term $\nu\nabla^2\omega$ in the vorticity transport equation for a viscous fluid can be treated exactly by using a Gaussian distribution,

$$\gamma_i(\mathbf{x} - \mathbf{r}_i) = \frac{\exp[-|\mathbf{x} - \mathbf{r}_i|^2/\sigma_i^2]}{\pi^{3/2}\sigma_i^3}, \tag{65}$$

with a viscous fattening of the core according to (18). This procedure should give satisfactory results for sufficiently low Reynolds numbers (ν large) although no published studies along this line are known at this time. For high Reynolds numbers, however, the space curves $\mathbf{r}_i(\xi, t)$ defining the vortex filaments may be subjected to significant localized stretching and distortion because of the large velocity gradients induced by the filaments with small cross section. These effects are, of course, a manifestation of turbulent flow. As discussed below, one normally would not have available the computational resources to describe accurately the motion of a collection of space curves with increasing regions of complex, fine-scale structure. Rather these simulations of medium to high Reynolds numbers should be carried out in the spirit of a large-eddy simulation [35, 36]. Here one computes approximately the dynamics of the large turbulent scales, while modeling the effect of the smaller, subgrid scales on the larger computed scales. In Eulerian simulations this is often accomplished simply by using a turbulent eddy viscosity that is constant, depends on the local rate of strain tensor, or on the vorticity:

$$\nu_T \sim \text{const.,} \tag{66}$$

$$\nu_T \sim \Delta^2 \, |S_{jk}|, \tag{67}$$

$$\nu_T \sim \Delta^2 \, |\omega|, \tag{68}$$

where Δ is the grid spacing for the Eulerian calculation. Similar techniques can and have been used in vortex methods. For example, (68) suggests a filament-dependent viscosity proportional to the circulation,

$$\nu_{T_i} \sim \Gamma_i. \tag{69}$$

Another interesting possibility for subgrid modeling, which has been investigated to a limited extent, is to allow for the generation of some fine-scale structure on the space curves. The situation is similar to that discussed in regard to the contour dynamics method. This behavior is most readily provided by allowing or remeshing the space curves as illustrated in Fig. 13. This permits the fine scales to develop in a natural way retaining some interplay between the large and small scales. An analogous procedure has seen only limited use in Eulerian calculations [37], probably because of the expense. In this case one must compute with a fine mesh everywhere and periodically filter out the high wavenumber components of the velocity or vorticity field.
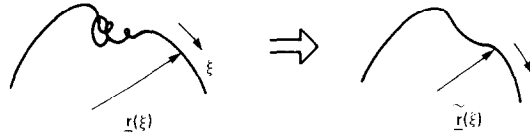
Fig. 13. Space curve with small-scale features, $r(\xi)$ and curve after smoothing $\tilde{r}(\xi)$.

Another manifestation of viscosity is the change in topology of closely interacting vortex loops. Experimental results [38, 39] and vortex simulations [40] show that filament loops in proximity may, depending on their relative orientation, attract each other to the extent that their vorticity fields are cancelled significantly where they overlap. It is postulated that under these circumstances their respective vortex lines become interwoven until viscous effects destroy the fine structure, thereby leaving no net vorticity in that neighborhood. From this process, a new geometric configuration arises, as illustrated in Fig. 14. Thus, if loops of two different vortex tubes collide, a single tube emerges; but if loops of the same tube undergo this process, two tubes emerge. In addition to the laboratory experiments cited above on interacting vortex rings, we note that by this process a pair of aircraft-trailing vortices might form a series of distorted vortex rings. The incorporation of this effect in a three-dimensional vortex method leads to troublesome bookkeeping problems but could yield substantial savings in the number of computational points for certain applications [40].

Finally, as discussed in Section 2, the presence of solid boundaries and the no-slip condition on the surface give rise to another important viscous effect—creation of vorticity at the surface. This new vorticity can be related to pressure gradients along the surface as follows. From the momentum equation evaluated at the wall we find that the increment in surface velocity $\delta \mathbf{u}_s$ generated in time δt is the sum of the two contributions,

$$\delta \mathbf{u}_s = \left(-\frac{1}{\rho} \nabla_s p + \nu \left. \frac{\partial^2 \mathbf{u}}{\partial \eta^2} \right|_s \right) \delta t \tag{70}$$

where $\nabla_s p$ is the gradient of the pressure on the surface, ρ is the fluid density, and η is the coordinate normal to the surface. The no-slip condition is satisfied when these two contributions cancel each other. The first term on the right-hand side of (70) is
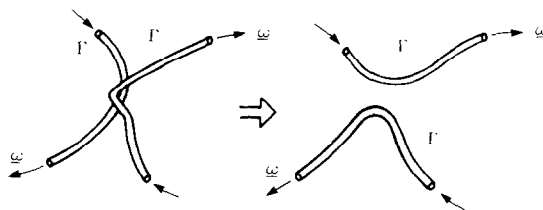

Fig. 14. Changing topology of vortex loops.

the slip generated in time δt by the inviscid motion of the fluid. The second term is related to the flux of vorticity through the surface because of the identity,

$$\left.\frac{\partial^2 \mathbf{u}}{\partial \eta^2}\right|_s = \mathbf{n} \times \frac{\partial \omega}{\partial \eta}, \tag{71}$$

where $\mathbf{n}$ is the unit outward normal at the surface. Combining (70) and (71) we find

$$-\nu \frac{\partial \omega}{\partial \eta} = \frac{1}{\rho} \mathbf{n} \times \nabla_s p. \tag{72}$$

Therefore, the vortex lines associated with this vorticity follow level curves of the surface pressure distribution, and the flux of circulation is proportional to the pressure gradient.

This result suggests a split scheme whereby the inviscid motion and the vorticity diffusion are computed as outlined above. Then the flux of vorticity through the boundary that results from these two substeps is computed. Finally new filaments are added at the boundary so that the net flux satisfies (72). A simpler scheme is to compute the slip generated by the first two substeps and then correct to zero slip by creating new filaments, i.e., the analog to the two-dimensional scheme given in Section 2.

To simulate three-dimensional flow past a sphere Leonard [41] used a simplified model of the boundary layer in which only certain integral properties were taken into account: (1) the net vorticity per unit area within the boundary layer is perpendicular to an equal in magnitude to the velocity at the edge of the boundary layer, $\mathbf{u}(\mathbf{r}_e)$, and tangent to the body surface,

$$\int_0^\delta \omega(\eta)\, d\eta = \mathbf{n} \times \mathbf{u}(\mathbf{r}_e); \tag{73}$$

and (2) the circulation within the boundary layer passing a given surface point per unit time in the streamwise direction is given by

$$\frac{d\Gamma}{dt} = -\int_0^\delta [\mathbf{n} \times \omega(\eta)]_\xi u_\xi(\eta)\, d\eta = \frac{|\mathbf{u}(\mathbf{r}_e)|^2}{2}. \tag{74}$$

Thus, the average vorticity in the boundary layer has an apparent speed of $|\mathbf{u}(\mathbf{r}_e)|/2$. In the model, the boundary-layer vorticity is divided into two parts: (1) an upstream attached layer of vorticity (composed of a single sheet) and (2) vortex filaments downstream of this sheet. The downstream boundary or front of the sheet moves with the local speed $|\mathbf{u}(\mathbf{r}_e)|/2$. When the front moves past a specified downstream latitude, a ribbon of the sheet is removed from the downstream edge and formed into a vortex filament (see Fig. 15). The height of the new filament above the surface is chosen so that the filament speed is $|\mathbf{u}(\mathbf{r}_e)|/2$, and the new position of the sheet front is deter-
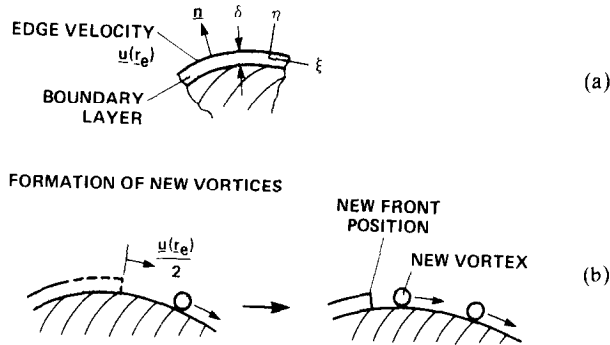
Fig. 15. Boundary-layer vorticity (a) description of terms for the boundary layer; (b) formation of new vortices from the attached sheet in the model of [41].

mined to maintain Eq. (74). In Leonard [41] the core size σ was chosen to maintain a relatively smooth representation of the boundary layer as in the mixing-layer simulation described in the previous section. A more refined technique might be to choose σ to preserve a precomputed momentum thickness or to preserve kinetic energy in the boundary layer [42]. Note that any vorticity production downstream of the edge of the sheet is ignored. Downstream of separation, however, vorticity production at the surface is known from experiment [43] to be small due to the nearly flat pressure coefficient in this region. The remaining error can be minimized by adjusting the cutoff latitude to be close to separation.

Recently, Chorin [44] has generalized his two-dimensional boundary-layer method using vortex sheets to three dimensions. Now the computational elements in the boundary layer are "tiles," which lie parallel to the surface and represent vortex sheets; the sheets are of finite length in the direction of the vorticity vector. Any local generation of slip can be cancelled by the creation of a new tile at that location with the proper strength and orientation. Away from the surface the tiles become finite tubes of vorticity—a technique used successfully by Rehbach [45] to simulate unsteady vortical flows past lifting surfaces in three dimensions. Although the solenoidal condition $\nabla \cdot \boldsymbol{\omega} = 0$ is only satisfied approximately, certain computational advantages are gained.

For most three-dimensional separated flow problems it might be sufficient to treat the turbulent boundary layer in terms of the boundary-layer equations with a turbulence model. Effects such as boundary-layer turbulence and external streamline curvature and their influence on the separation process could be represented in a realistic fashion.

E. Applications of the Vortex Filament Method

The first application of the three-dimensional vortex filament method is to the simulation of the interaction of aircraft-trailing vortices. Studies of this type are primarily motivated by the hazards to which light aircraft are exposed when flying in the wake of a heavier aircraft—a wake that may contain vortices with large

circulations and small cores. In such cases, following aircraft may be subjected to a very high rolling moment when they encounter one of these vortices.

One possible method of alleviating this hazard is to provide a wing loading that produces multiple trailing vortices from each wing. It is hoped that by proper adjustment of the positions and strengths of these vortices (through the loading distributions on the wing), a strong interaction and merging of these vortices will occur a short distance downstream, resulting in a single vortex with a very large, diffuse core.

A schematic of the numerical simulation of this interaction process is shown in Fig. 16. An independent calculation (e.g., by a vortex lattice method) or experiment is required to determine the filament circulations, Γ_i, the core sizes σ_i of the filaments, and the locations (y_i, z_i) of the filaments in the plane just downstream of the roll-up. The computational domain extends from this plane to a plane downstream of the region of interest. During the simulation, points are added continually at this trailing-edge plane as the other computational points are moving downstream with an average speed of U_∞. For numerical treatment of the Biot–Savart integration (55) the space curves, curves, $\mathbf{r}_i(\xi, t)$, are assumed to be piecewise linear between successive computational points. (In unpublished work, D. Degani and the author (1976) investigated the use of cubic spline representations for the space curves. The were found useful for remeshing purposes and for obtaining integration schemes with higher order accuracy at some additional computing effort.) Downstream of the computational domain semi-infinite vortex filaments are used as shown in Fig. 16 to account for the incremental velocity induced on the computational points from wake vorticity in this downstream region. This situation is completely analogous to that in the two-dimensional mixing-layer simulation of the previous section. Velocity contributions from the potential flow and wake due to the fuselage were neglected in the simulation.

Because of the availability of experimental data, the wake of a Boeing 747 wing
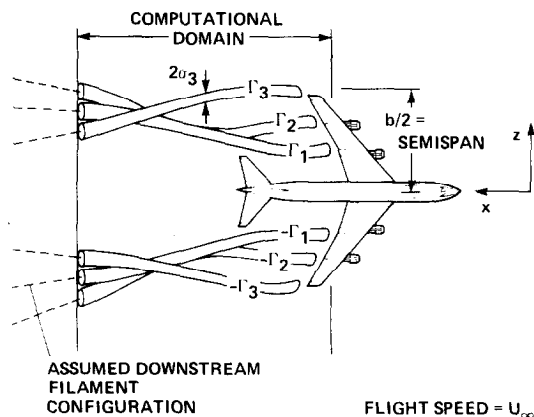

FIG. 16.   Simulation of aircraft-trailing vortices.

with inboard flaps at 30° was simulated. (See Hackett and Evans [46] for similar studies of aircraft wakes and Moore [30] for a simulation of the instability between two counterrotating tip vortices.) The span loading as predicted by a vortex lattice method is shown in Fig. 17. Based on this loading pattern one would expect three vortices on each halfspan to emerge from the roll-up process immediately downstream of the trailing edge of the wing— two vortices of opposite sign produced by the flap and one vortex from the tip. This is verified by experiment. For this simulation the initial conditions, Γ_i, σ_i, and (y_i, z_i), were obtained from laser velocimeter measurements in the wind tunnel [47].

The results of a water tunnel experiment [48] using flow visualization with dye to follow the motion of the wake vortices were available for comparison with the simulation. Figure 18 shows the computed configurations of the filaments after initial transients in the simulation have settled out. Note the upward and inward motion of the tip vortex which initially is primarily influenced by the stronger outboard flap vortex. The inboard flap vortex is seen to suffer an instability in agreement with flight tests [49]. The simulated and measured trajectories of the tip vortex about the outboard flap vortex in the cross-sectional plane are shown in Fig. 19. The agreement is quite good on this very sensitive quantity. As a comparison also shown are the results of a vortex simulation using initial conditions estimated from a vortex lattice calculation and additional computational procedures. Note that in this case, the stimulated results were not satisfactory. The tip vortex revolved clockwise about but away from the flap vortex as shown in Fig. 19. Experimentally this sensitivity was demonstrated by the fact that for the 30° flap configuration a beneficial merging of the vortices occurs with landing gear up but not for the landing gear down [47].

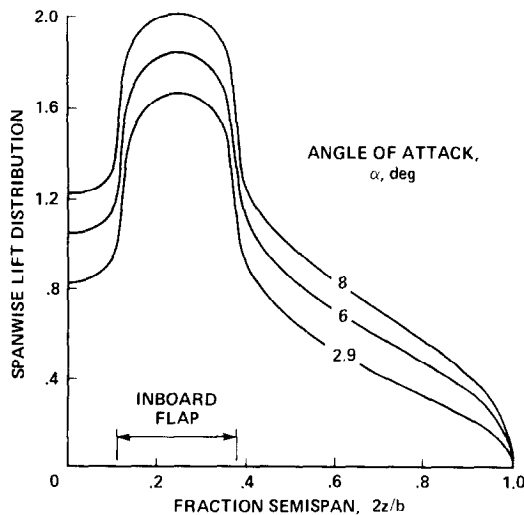For a second example we present selected results of a simulation of a three-

FIG. 17.   Vortex lattice calculation of lift distributions for a Boeing 747.

TIP

FLAP OUTBOARD

FLAP INBOARD

TIP

FLAP OUTBOARD

FLAP INBOARD

(a) TOP VIEW

TIP

FLAP OUTBOARD   FLAP INBOARD

TIP
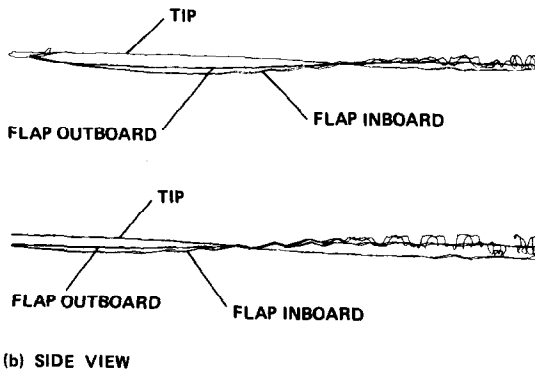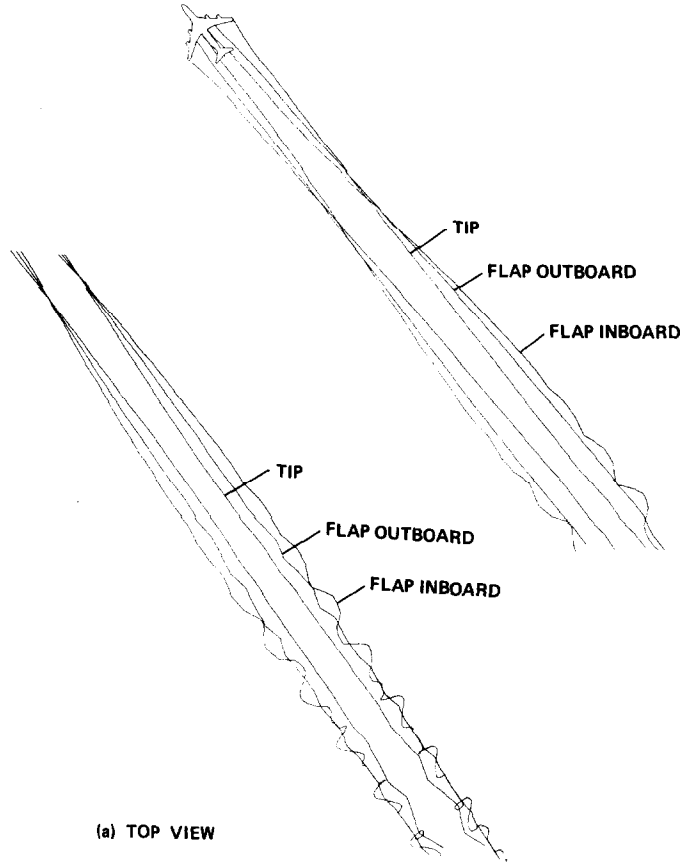
FLAP OUTBOARD   FLAP INBOARD

(b) SIDE VIEW

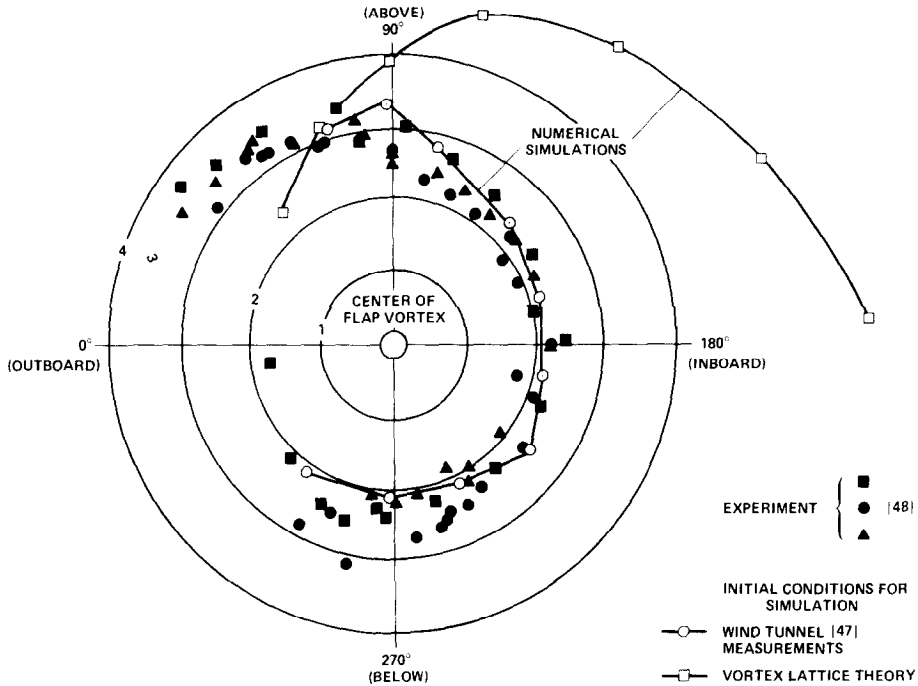FIG. 18.   Vortex filaments in the simulation of the wake of a Boeing 747.

FIG. 19.   Trajectories of the wing-tip vortex from experiment and vortex simulation.

dimensional spotlike disturbance in a laminar boundary layer [31]. In this case the vortex filaments must represent a continuum of vorticity which initially is in the form of an infinite sheet of finite thickness, i.e., a boundary layer. The numerical simulation follows the evolution of a small localized disturbance in the layer as it grows by linear and nonlinear interactions. As indicated in the schematic (Fig. 20)
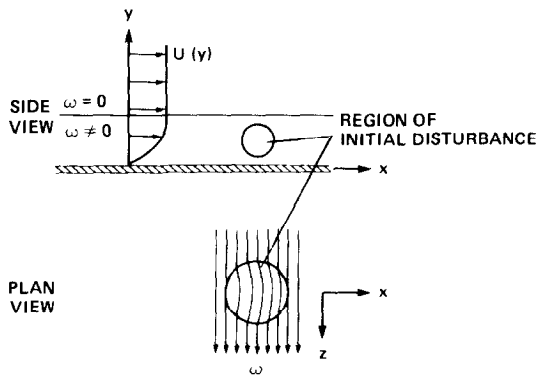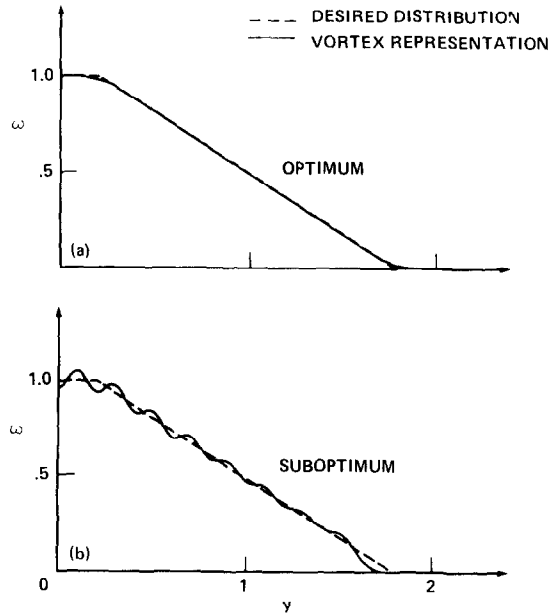

FIG. 20.   Spot geometry.

FIG. 21. Vorticity distributions: (a) optimum vortex representation; (b) suboptimum choice of core size.

the disturbance in the simulation is created by a local distortion of the vortex filaments at $t = 0$. The boundary layer is represented by six layers of vortex filaments. By proper choice of the σ_i and Γ_i for each layer the desired vorticity distribution can be well approximated, as indicated in Fig. 21. Computed filaments are added automatically as the disturbance grows in size. The numerical procedures used are essentially those of the previous example except that image contributions are computed to satisfy the inviscid boundary condition. The generation of new vorticity at the wall due to the no-slip condition is ignored. At the end of the simulation about 8000 points represent one half of the spot (symmetry of the flow about the midplane was enforced). Run times are 1–2 hr on the ILLIAC.

In Fig. 22, the space curves defining the vortex filaments in a single layer are shown at three different times. The spreading of the disturbance and the increasing deformations suffered by the vortex lines are quite evident. From the space curves defined by the computational grid of node points we can generate vorticity/velocity field information as desired (cf. Eqs. (48) and (53)). For example, vorticity and velocity contour plots in the horizontal plane are shown in Fig. 23, and in Fig. 24 we show a streamwise vorticity contour plot for a spanwise-vertical plane. (In each case only one half of the spot is shown because of symmetry.) Note the appearance of intense streamwise and vertical vorticity generated in the flow in agreement with the pattern of vortex lines displayed in Fig. 22. The presence of streaky structures in the u' and v plots in the horizontal plane is in agreement with experimental observations

of turbulent boundary layers. Other comparisons with experimental results on turbulent spots, such as the propagation speed of the disturbance, are also quite encouraging.

Other investigations of three-dimensional boundary layer phenomena by vortex methods include an early study by Hama [50] who, motivated by his experimental observations of boundary layer transition, computed the motion of a single vortex
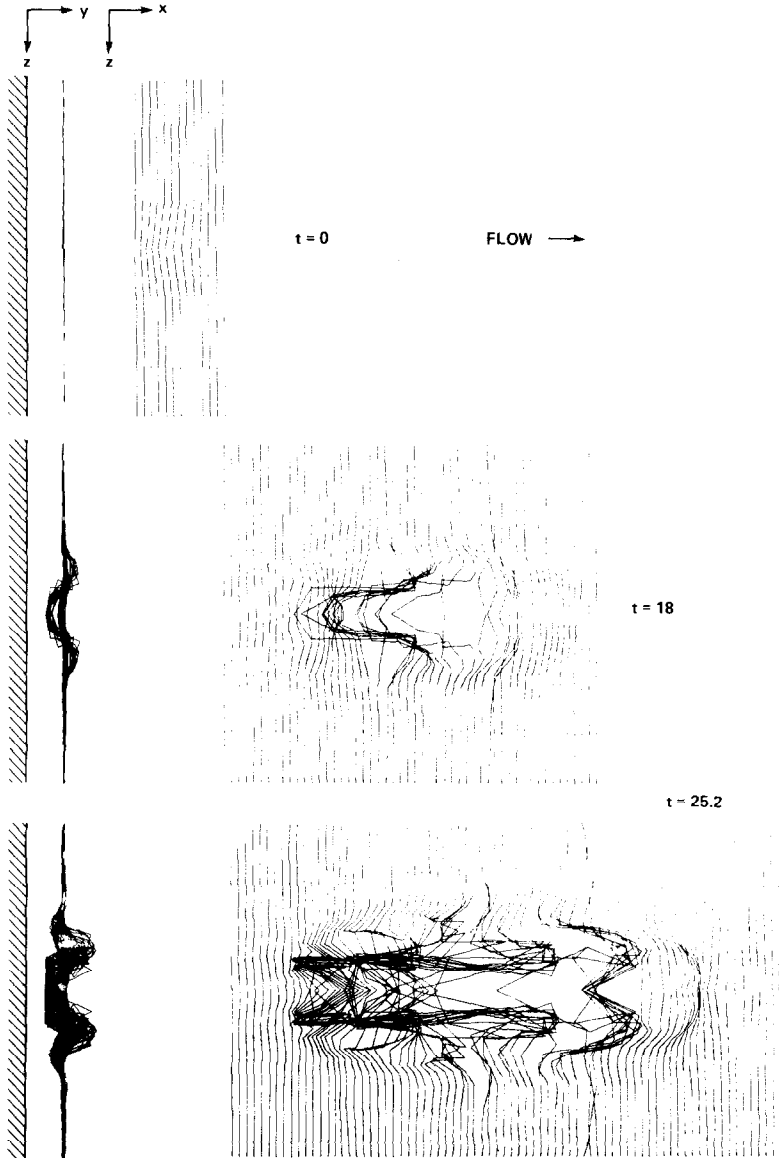

FIG. 22. Top and rear views of one plane of the computed vortex lines.

loop. Recently, Chorin [44], using the "tile" method described earlier, studied boundary layer instability.

Other applications in three dimensions include Del Prete's study [51] of vortex breakdown, the author's simulation [41] of flow past a sphere, and Meng's investigation [52] of the evolution of a vortex ring in a stratified and shearing environment. In Meng's study, modifications to the basic method were required to account for vorticity sources due to density stratification.
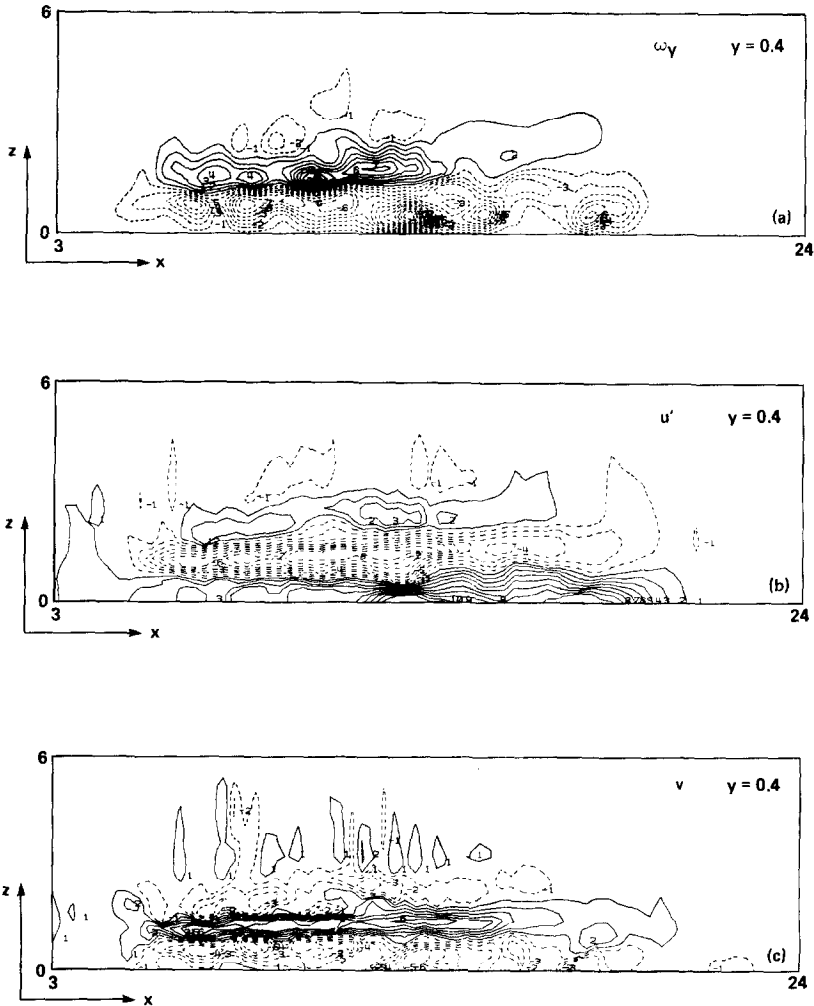

FIG. 23.   Contour plots in the horizontal plane, $y = 0.4$, $t = 24$. (a) ω_y; (b) u', perturbation in streamwise velocity; (c) v, vertical velocity.
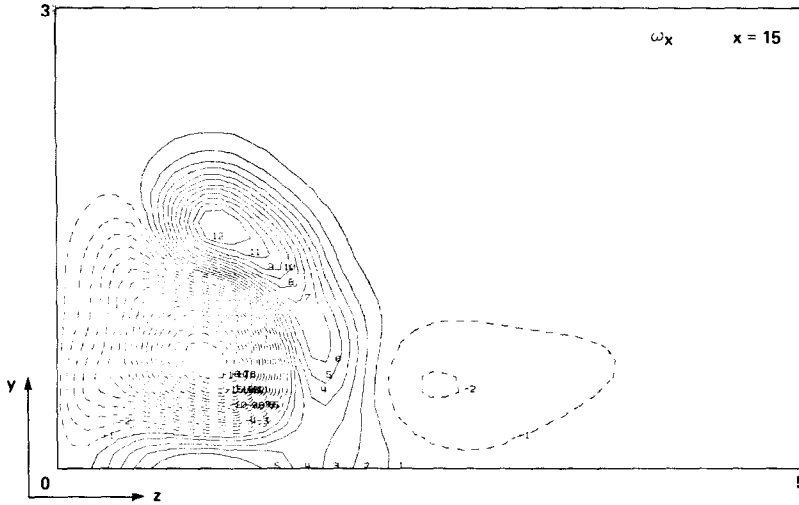
FIG. 24. Contour plot of streamwise vorticity in a spanwise-vertical plane.

4. VORTEX-IN-CELL METHODS

In the vortex methods described above the velocities required to move the computational elements each time step are essentially computed by a Green's function solution to the Poisson equation (6) or (51). For N computational elements or points this procedure requires $O(N^2)$ operations to compute all the required velocities. This places a rather modest upper limit on the number of elements that can be used if about 1 hr of CPU time for a given problem is allowed. Experience has shown this limit to be $N \approx 1000$–2000 for a CDC 7600 and 4000–8000 for ILLIAC. Depending on the application, various shortcuts can be used to decrease the computing time, such as combining a number of elements in a given region into a pseudoelement to compute their influence on distant points.

In this section we discuss a systematic approach to the problem which results in what are termed vortex-in-cell methods. The idea is to retain the Lagrangian treatment of the vorticity field but to solve the Poisson equation for the velocity field on a fixed Eulerian mesh. By use of fast Poisson solvers on a mesh of M grid points, the operation count for this step can approach $O(M \log M)$. Additional required steps are (1) the generation of mesh values for the vorticity field from the Lagrangian representation and (2) interpolating velocities from the mesh back into the Lagrangian points. As we shall see these two steps require only $O(N)$ operations per step. Therefore we find that the computing time per step for the two methods is as follows:

$$\text{Direct interaction: CPU time/step} \approx C_1 N^2$$

$$\text{Vortex-in-cell: CPU time/step} \approx C_2 N + C_3 M \log_2 M$$

Depending on the problem, the number of mesh points, M, required could be $O(N)$ or much larger.

A. *Cloud-in-Cell Method*

We now describe a particular way to implement these ideas in two dimensions, called the could-in-cell (CIC) method [53]. A given vortex, say at (x_n, y_n) with circulation Γ_n, resides within a certain mesh cell, as depicted in Fig. 25, and contributes incremental vorticity, $\delta\omega(l)$, to each of the four mesh points at the corners ($l = 1, 2, 3, 4$) according to the area weighting scheme,

$$\delta\omega(l) = A_l \Gamma_n / h^2, \tag{75}$$

on a side within which the vorticity is constant. Any vorticity that is within the region defined by

$$x_i - \frac{h}{2} < x \leqslant x_i + \frac{h}{2},$$

$$y_i - \frac{h}{2} < y \leqslant y_i + \frac{h}{2}, \tag{76}$$

"belongs" to the mesh point (i, j). After all the vorticity has been distributed among the mesh points a finite difference form of the Poisson equation for the stream function, ψ, is solved. For example, one might solve

$$\left(\frac{\delta^2}{\delta x^2} + \frac{\delta^2}{\delta y^2} \right) \psi_{i,j} = -\omega_{i,j}, \tag{77}$$

where $\delta^2/\delta x^2$ and $\delta^2/\delta y^2$ are the three-point central difference operators. If the flow is not periodic, boundary conditions for the stream function may need to be computed (see Baker [54] for a discussion of various possibilities). With the stream function in
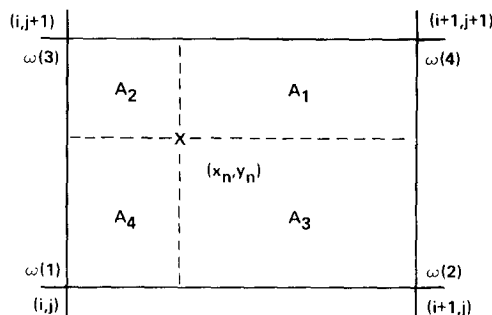

FIG. 25.   Area weighting scheme for the cloud-in-cell method (after [54]).

hand, velocities at the mesh points can be calculated, for example, by central differences,

$$u_{i,j} = \frac{\psi_{i,j+1} - \psi_{i,j-1}}{2h}$$

and   (78)

$$v_{i,j} = -\frac{\psi_{i+1,j} - \psi_{i-1,j}}{2h},$$

and then bilinear interpolation (area weighting) can be used to determine the velocity of vortex n,

$$\mathbf{u}_n = \sum_{l=1}^{4} \mathbf{u}(l)\frac{A_l}{h^2},$$ (79)

and of all the other vortices. Clearly, the distribution of vorticity to the mesh and the interpolation of mesh velocities onto the vortices require only a fixed number of operations per vortex (independent of M or N) so that the operation count per time step for this portion of the computation is $O(N)$.

Using the CIC method, Christiansen [53] reported a number of interesting
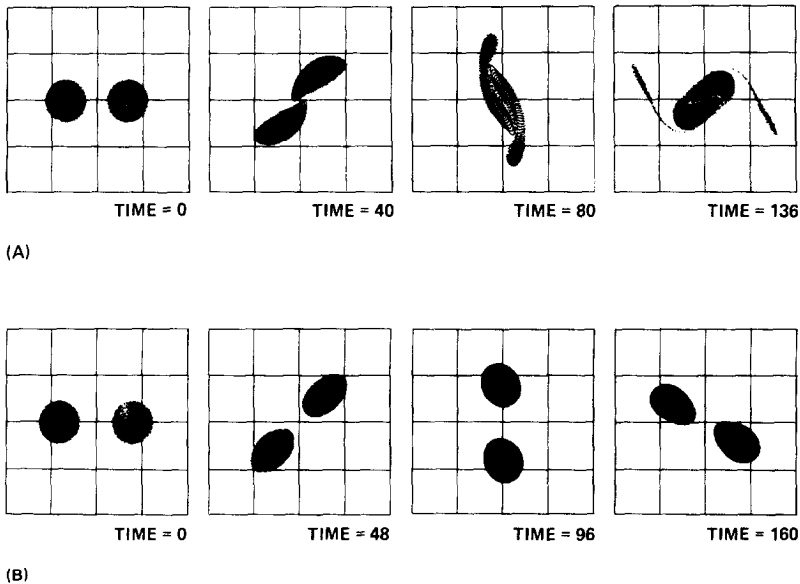

FIG. 26. Precession of two finite-area vortices as computed by the cloud-in-cell method [53]. (a) Small initial separation; (b) larger initial separation. (Permission to use figure granted by Dr. J. P. Christiansen.

demonstration calculations. The results of two of his cases concerning the dynamics of two finite-area regions of vorticity in proximity are reproduced in Fig. 26. The vortices, having the same circulation, precess about each other. Depending on their initial separation, they either coalesce (Fig. 26a) or they do not (Fig. 26b). In these simulations, ψ is assumed periodic in x and constant along the y boundaries. The computation was on a 64×64 mesh with approximately 3000 vortices.

Figure 27 shows the simulation by Baker [54] of the roll-up of a vortex sheet. A total of 1950 vortices are used in a 129×129 mesh. Only half the points are shown in this symmetric problem. Each vortex has the same magnitude of circulation. The initial spacings between the vortices are chosen to represent the desired initial
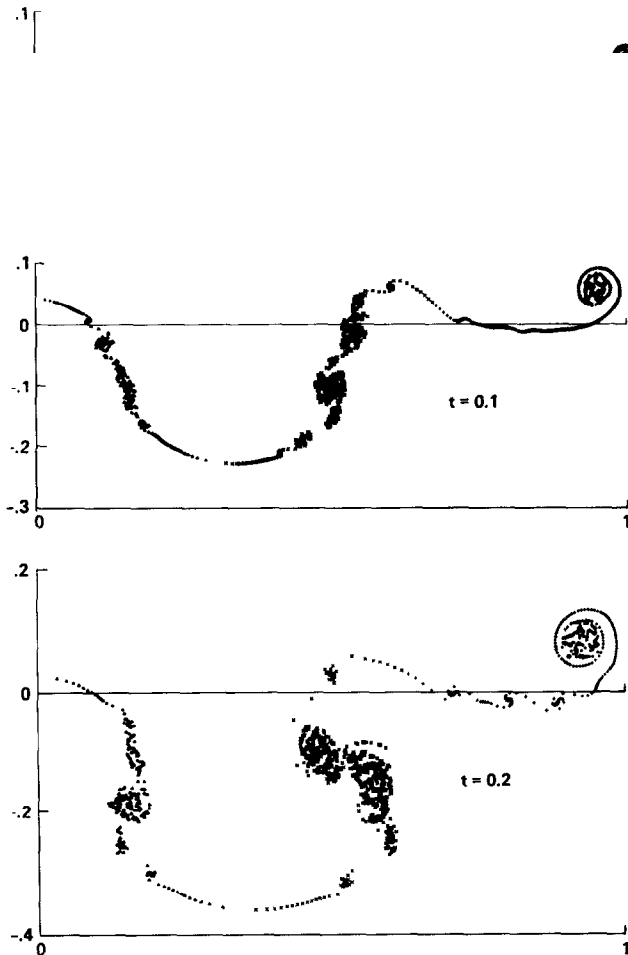

FIG. 27.   Cloud-in-cell simulation of the roll-up of a vortex sheet [54]. (Permission to use figure granted by Gregory R. Baker.)

vorticity distribution along the sheet. In the case shown, this distribution is chosen to simulate a vortex sheet shed from a wing with a flap deployed. The span loading is qualitatively similar to the one shown in Fig. 17.

B. *Error Considerations*

The hybrid scheme described above introduces several sources of error in addition to those discussed in connection with the vortex blob method. The distribution of vorticity to the mesh and the interpolation to obtain vortex velocities are subject to error, as are the differencing procedures used to solve the Poisson equation and determine the mesh velocities. Numerical studies by Christiansen [53] and Baker [54] point to the anisotropic nature of the distribution and interpolation schemes as the most significant new source of error. To give an example, a straight section of a vortex sheet at an angle to the mesh lines will distribute vorticity to the shaded mesh cells, as shown in Fig. 28 [54] Relatively large perturbations due to the mesh are then produced on a scale comparable to the distance AB. This effect will often produce fine-scale structures, scaled by the mesh spacing, that are quite noticeable, say, in the vorticity distribution. Another indication of the existence and nature of this error is the fact that while the total circulation and linear impulse are conserved by the CIC method, angular impulse is not. However, numerical experiments in two dimensions [54] indicate that although these fine-scale errors are present they may not seriously affect the large-scale features. The latter seem to be mesh independent.

C. *Improved Techniques*

One proposal to improve the numerics of the CIC method has been put forth by Hockney *et al.* [55]. Rather than using area weighting to the nearest four mesh points, or equivalently, vortices with square, constant-vorticity cores $(h \times h)$, these authors propose the use of a truncated Gaussian core having a larger cross section $(2h \times 2h)$,

$$\gamma(\mathbf{x} - \mathbf{x}_n) \propto \begin{cases} \exp[-|\mathbf{x} - \mathbf{x}_n|^2/\sigma^2], & |x - x_n| \leqslant h, \quad |y - y_n| \leqslant h, \\ 0, & \text{otherwise,} \end{cases}$$
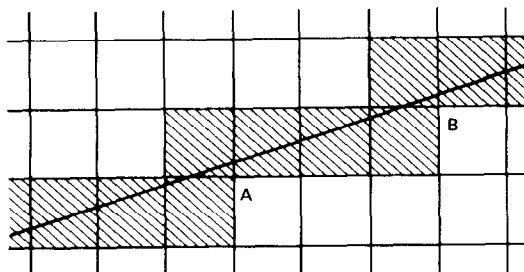

FIG. 28. Mesh cells involved in the distribution process [54].

with $\sigma = 0.643h$. This element contributes vorticity to the surrounding nine mesh points rather than to the nearest four. The interpolated velocities use the same nine weight factors so that the method approximates the pure Lagrangian scheme B of Section 2. Any residual errors produced by the squareness of the mesh plus the finite difference errors are nearly eliminated by adjusting, in Fourier transform space, the Green's function of the discrete Laplace operator. Hockney *et al.* state that mesh errors are reduced by two orders of magnitude by these improvements.

In Buneman [56–58] the Poisson equation for the fully periodic velocity field in two dimensions is solved by Fourier methods to obtain

$$\hat{\mathbf{u}}(\mathbf{k}) = \frac{i}{k^2} (\mathbf{k} \times \hat{e}_z) \,\hat{\omega}(\mathbf{k}) \tag{80}$$

for the Fourier transform of the velocity field in discrete $\mathbf{k}$ space. Because Fourier methods are used there is no need to correct for finite difference errors. The construction of $\omega(\mathbf{k})$ follows by noting that the Fourier transform of (9) with the same distribution γ for all vortices gives

$$\hat{\omega}(\mathbf{k}) = \hat{\gamma}(\mathbf{k}) \sum_{n=1}^{N} \Gamma_n \exp[-i\mathbf{k} \cdot \mathbf{x}_n], \tag{81}$$

implying $O(NM)$ operations to determine $\hat{\omega}(\mathbf{k})$ (M is the number of Fourier modes). This operation count is reduced to $O(N)$, however, by approximating $\exp[i\mathbf{k} \cdot \mathbf{x}_n]$ by a linear combination of $\exp[i\mathbf{k} \cdot \mathbf{x}(i,j)]$, where the $\mathbf{x}(i,j)$ are Eulerian grid points neighboring $\mathbf{x}_n$, and by using fast Fourier transform (FFT) methods.

This approximation in each direction is taken as the best spline fit [58], namely, for linear spline interpolation with x between integer grid points n and $n+1$,

$$e^{ikx} \approx S_1(k)[(n+1-x)\,e^{ikn} + (x-n)\,e^{ik(n+1)}], \tag{82a}$$

or, for quadratic spline interpolation with $n - \frac{1}{2} \leqslant x \leqslant n + \frac{1}{2}$,

$$e^{ikx} \approx S_2(k)\{\tfrac{1}{2}(n+\tfrac{1}{2}-x)^2\,e^{ik(n-1)} + [\tfrac{3}{4} - (x-n)^2]\,e^{ikn}$$
$$+ \tfrac{1}{2}(x-n+\tfrac{1}{2})^2\,e^{ik(n+1)}\}, \tag{82b}$$

and similarly for cubic and higher-order splines. The factors $S_i(k)$ are chosen to minimize the rms error of the approximation over all positions x between two mesh points. The functions $S_1(k)$ and $S_2(k)$ are found to be

$$S_1(k) = \left(\frac{2}{k}\sin\frac{k}{2}\right)^2 \Big/ \left(1 - \frac{2}{3}\sin^2\frac{k}{2}\right) \tag{83a}$$

and

$$S_2(k) = \left(\frac{2}{k}\sin\frac{k}{2}\right)^3 \Big/ \left(1 - \sin^2\frac{k}{2} + \frac{2}{15}\sin^4\frac{k}{2}\right). \tag{83b}$$

In the method utilizing quadratic splines, for example, each vortex contributes vorticity in real space to the three nearest neighbor mesh points in each direction (9 total in 2D, 27 total in 3D) according to the coefficients to the spline fit given in (82b). Then an FFT of the x-space field is taken. In k-space the application of the factors $S_2(k)$ in each direction and the shape factor $\hat{\gamma}(\mathbf{k})$ as well as the Poisson solution for $\hat{\mathbf{u}}(\mathbf{k})$ are simple multiplicative operations. The procedure essentially is reversed to determine $d\mathbf{x}_n/dt$ from $\hat{\mathbf{u}}(\mathbf{k})$.

The rms errors in the approximations (82) are shown in Fig. 29 versus wave number [59]. The effect of the errors shown at the higher wave numbers can be minimized by choosing a $\hat{\gamma}(\mathbf{k})$ that is small for large k or equivalently a relative large core size σ. One must, therefore, find a balance between decreasing the error due to the mesh (by increasing σ) and decreasing the error of the vortex blob method (by decreasing σ). Buneman [57] has demonstrated nearly complete insensitivity to the underlying mesh using cubic splines and $\hat{\gamma}(\mathbf{k}) = \exp(-3h^2 k^2/\pi^2)$. Wang [60] used this technique to study the dynamics of the two-dimensional mixing layer.

D. *Three-Dimensional Vortex-in-Cell Method*

Buneman *et al.* [61] have developed a vortex-in-cell method in three dimensions utilizing quadratic splines with vortex filaments to represent the vorticity field. From (48), with the distribution γ the same for all filaments, we see that the transform of the vorticity field is given by

$$\hat{\omega}(\mathbf{k}) = \hat{\gamma}(\mathbf{k}) \sum_{j=1}^{L} \Gamma_j \int e^{-i\mathbf{k} \cdot \mathbf{r}_j(\xi,t)} \frac{\partial \mathbf{r}_j}{\partial \xi} d\xi. \tag{84}$$

If each space curve is approximated by straight line segments between computational points denoted by $\mathbf{r}_{j,l}$ ($l = 1,\ldots, N_j$) and the integration between each pair of points is accomplished by two-point Gauss–Legendre quadrature, we find

$$\hat{\omega}(\mathbf{k}) = \hat{\gamma}(\mathbf{k}) \sum_{j=1}^{L} \Gamma_j \sum_{l=1}^{N_j} \tfrac{1}{2}(\mathbf{r}_{j,l} - \mathbf{r}_{j,l-1})$$

$$\times \left[\exp(-i\mathbf{k} \cdot \mathbf{r}_{j,l}^-) + \exp(-i\mathbf{k} \cdot \mathbf{r}_{j,l}^+)\right], \tag{85}$$
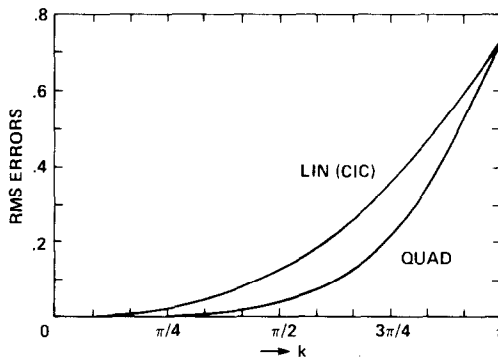

FIG. 29. Root-mean-square error in the spline interpolation of exp(*ikx*) [59].

where $\mathbf{r}_{j,0} = \mathbf{r}_{j,N_j}$ and the quadrature points $\mathbf{r}_{j,l}^{\pm}$ are defined by

$$\mathbf{r}_{j,l}^{\pm} = \tfrac{1}{2}[(1 \pm \tfrac{1}{3}^{1/2})\,\mathbf{r}_{j,l} + (1 \mp \tfrac{1}{3}^{1/2})\,\mathbf{r}_{j,l-1}]. \tag{86}$$

At this point the computation proceeds as in two dimensions except that each Gauss quadrature point yields vector contributions to 27 neighbors in real space. The method approximates the pure Lagrangian scheme D of Section 3.

Tests of the three-dimensional vortex-in-cell method have indicated only minimal grid effects and no numerical instabilities. For example, comparisons were made with a pure Lagrangian calculation of the propagation of a periodic system of ring vortices [61]. Due to the Cartesian placement of the image system of vortex rings the propagation speed is a function of azimuth. In Fig. 30 the vortex-in-cell results for a 16^3 mesh are compared with those of the Lagrangian scheme to determine the error due to mesh effects. Only a small, high-frequency error (rms ≈ 1 %) is noted.

A number of applications are being studied [59, 62]. In Fig. 31, for example, the vortex filaments are shown from a mixing-layer simulation with a single harmonic
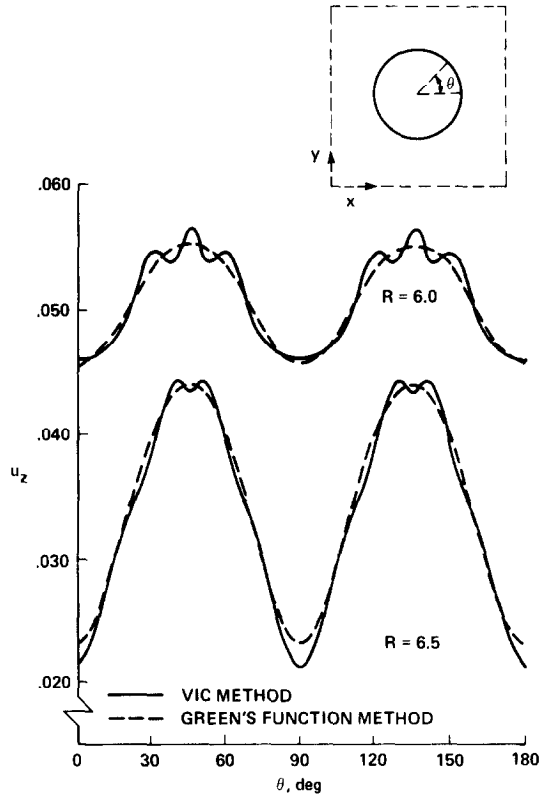

FIG. 30. Velocity of translation versus the angle θ around the ring for a periodic array of single vortex rings: $\Gamma = 2.0$.
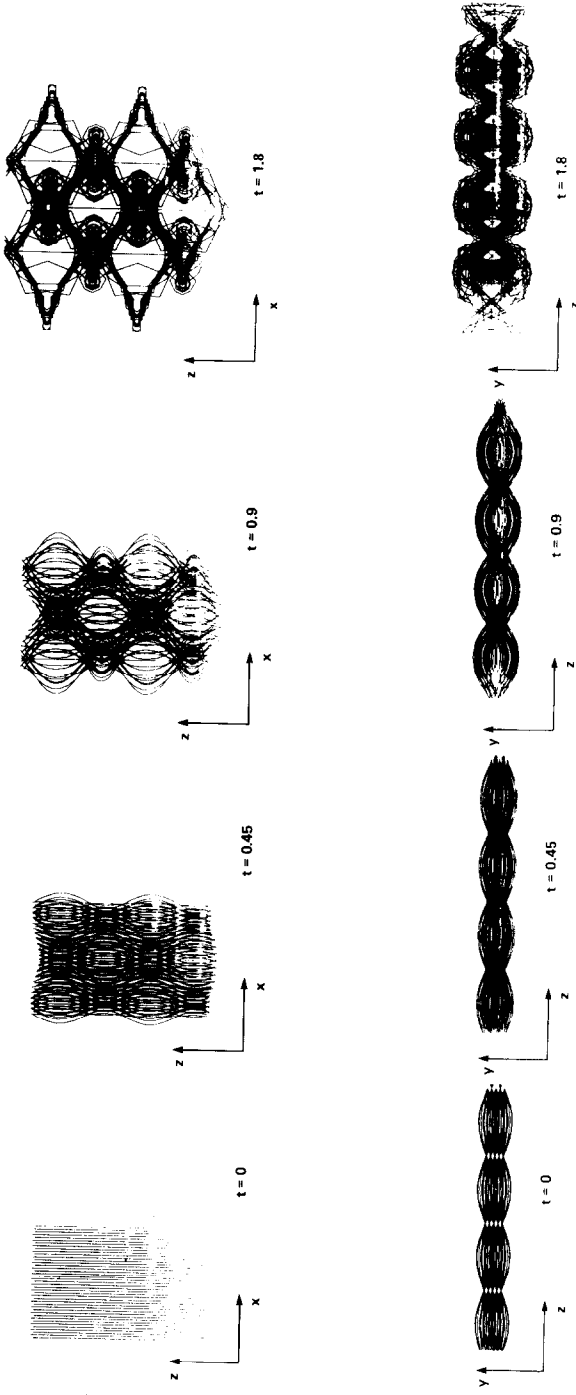
FIG. 31.   Vortex lines for 3-D perturbation of the mixing layer.

initial disturbance in the spanwise and streamwise directions. The mesh is 32^3 with
5120 points in 160 filaments representing the mixing layer. Work is also under way
to relax the requirement of periodicity in all three directions and to implement a
remeshing scheme [62].

Finally we note that Hockney *et al.* [55] have proposed additional procedures to
accommodate vortices with arbitrary core distributions. They call this the PPPM
(paticle–particle/particle–mesh) method. The method is based on the observation that
only nearby vortices can "see" the difference between the actual structure of a given
vortex and the structure endowed upon the vortex by the vortex-in-cell method. A
vortex–vortex correction must therefore be made between all vortices within a certain
distance, $O(h)$, of each other. Construction of a linked list of vortex labels facilitates
the computation of these close interactions.

5. SUMMARY AND CONCLUSIONS

Vorticity moves with the local velocity in the inviscid motion of a fluid. If the flow
is incompressible, knowledge of the vorticity distribution is sufficient to determine the
velocity field. Vortex methods essentially represent a direct translation of these facts
to a numerical algorithm for flow simulation.

Vortex methods offer a number of advantages over the more traditional Eulerian
schemes. But as might be expected each advantage seems to be offset by a
corresponding disadvantage. It is the goal of the practitioner to exploit the advantages
to the fullest possible extent while finding means of circumventing the disadvantages.
Four advantages and their side effects are cited below:

1. Because computational points are required only in the rotational parts of the
flow, vortex methods use a minimal description of the flow field which is pleasing
theoretically and requires only a relatively small number of storage locations. The
three flow problems described in this paper provide good examples of this aspect of
vortex methods. Other examples include flow simulations of aerodynamic bodies at
high angle of attack, using only a few vortices but obtaining aerodynamic forces of
sufficient accuracy for engineering purposes [63]. On the other hand, the number of
operations per time step is roughly proportional to the square of the number of vortex
elements or coordinates in the discretization, rapidly leading to excessive computation
times as the number of elements is increased.

2. The Lagrangian treatment eliminates the need to explicitly treat convective
derivatives. Because of this, small-scale features can often be convected accurately
with a relatively large time step and certain singular distributions in vorticity may be
treated exactly by the method. The errors generated in representing smooth flows are
not well understood, however, and the treatment of viscous effects can be
troublesome.

3. In turbulent fluid flows and in many high Reynolds number laminar flows,
fine-scale structures may develop in an intermittent manner throughout the flow field.

Vortex methods can automatically allow such regions to develop by a local concentration of computational points. Due to limited resources, however, remeshing will often be required with all the concomitant difficulties and approximations.

4. Boundary conditions at infinity may be treated exactly, and accurate outflow boundary conditions are available and easy to implement. On the other hand, no-slip conditions at a solid wall require much care.

A number of proposals aimed at minimizing the disadvantages cited in items 1–4 above were presented and discussed in this paper. Comments, some definite and some speculative, can now be made about these proposals. With regard to the computational effort noted in item 1, vortex-in-cell methods can be used to improve dramatically the computational efficiency if a large number of vortex elements are required. In connection with the errors of vortex methods mentioned in item 2, recall that the spatial truncation error is not diffusive, as shown by the analysis in Section 2 and the mixing-layer simulation. This property is useful in a number of applications, for example, in the model piston–cylinder problem of Ashurst [64], in which the shear layers emanating from the valves are well represented. In other words, the nondiffusive nature of the error can be exploited. In addition, vortex methods with high-order spatial accuracy are possible, as discussed in Section 2. These schemes should be tested and extended to three dimensions.

The contour dynamics method in two dimensions and the vortex filament method for three-dimensional flows use computational points to define space curves. Reference was made in item 3 to the negative aspects of remeshing these curves. On the positive side, it seems that there is a definite connection between the remeshing process and the cascade of turbulent energy to smaller scales and hence a connection to a meaningful subgrid model. Finally, it is noted that several alternatives of varying degrees of complexity and approximation exist for the treatment of the no-slip boundary condition and the subsequent mechanics of the boundary layer. Further numerical experimentation and analysis is needed to determine the efficacy of these alternatives.

REFERENCES

1. R. R. CLEMENTS AND D. J. MAULL, *Prog. Aerospace Sci.* **16** (1975), 129–146.
2. P. T. FINK AND W. K. SOH, *in* "Proceedings, 10th Symp. Nav. Hydrodyn., Cambridge, Mass., 1974," pp. 463–488.
3. P. G. SAFFMAN AND G. R. BAKER, *Ann. Rev. Fluid Mech.* **11** (1979), 95–122.
4. D. J. MAULL, "An Introduction to the Discrete Vortex Method," IUTAM/IAHR, Karlsruhe, 1979.
5. L. ROSENHEAD, *Proc. Roy. Soc. London A* **134** (1931), 170–192.

6. G. BIRKHOFF AND J. FISHER, *Circ. Mat. Palermo* **8** (1959), 77–90.

7. D. W. MOORE, *Mathematika* **23** (1976), 35–44.

8. A. J. CHORIN, *J. Fluid Mech.* **57** (1973), 785–796.

9. A. J. CHORIN AND P. S. BERNARD, *J. Comput. Phys.* **13** (1973), 423–428.

10. O. H. HALD, *SIAM J. Numer. Anal.* **16** (1979), 726–755.

11. A. LEONARD, "On the Accuracy of Vortex Methods," in preparation.

12. O. H. HALD AND V. M. DEL PRETE, *Math. Comput.* **32** (1978), 791–809.

13. W. T. ASHURST, *in* "Turbulent Shear Flows, I" (F. Durst *et al.*, Eds.), pp. 402–413, Springer-Verlag, Berlin, 1979 also "Numerical Simulation of Turbulent Mixing Layers Via Vortex Dynamics" Sandia Laboratories, SAND77-8613, Livermore, CA, Feb. 1977.

14. F. MILINAZZO AND P. G. SAFFMAN, *J. Comput. Phys.* **23** (1977), 380–392.

15. A. J. CHORIN, *J. Comput. Phys.* **26** (1978), 453–454.

16. P. G. SAFFMAN, *J. Comput. Phys.* **26** (1978), 455–456.

17. T. SARPKAYA, *J. Fluid Mech.* **68** (1975), 109–128.

18. M. KIYA AND A. ARIE, *J. Fluid Mech.* **82** (1977), 241–253.

19. A. J. CHORIN, T. J. R. HUGHES, M. F. MCCRACKEN, AND J. E. MARSDEN, *Comm. Pure Appl. Math.* **31** (1978), 205–256.

20. R. S. ROGALLO, *in* "Proceedings, 2nd Computational Fluid Dynamics Conference, AIAA, 1975," p. 67.

21. A. I. SHESTAKOV, *J. Comput. Phys.* **31** (1979), 313–334.

22. A. J. CHORIN, *J. Comput. Phys.* **27** (1978), 428–442.

23. A. CHEER, "A Study of Incompressible Two-Dimensional Vortex Flow Past a Circular Cylinder," Lawrence Berkeley Laboratory Report LBL-9950, July 1979.

24. E. ACTON, *J. Fluid Mech.* **76** (1976), 561–592.

25. N. J. ZABUSKY, M. H. HUGHES, AND K. V. ROBERTS, *J. Comput. Phys.* **30** (1979), 96–106.

26. G. S. DEEM AND N. J. ZABUSKY, *in* "Solitons in Action," pp. 277–294, Academic Press, New York, 1978.

27. J. NORBURY, *J. Fluid Mech.* **57** (1973), 417–431.

28. S. WIDNALL, D. BLISS, AND A. ZALAY, *in* "Aircraft Wake Turbulence and Its Detection," p. 305, Plenum, New York, 1971.

29. D. W. MOORE AND P. G. SAFFMAN, *Phil. Trans. Roy. Soc. London* **272**(1972), 403–429.

30. D. W. MOORE, *Aeronaut. Q.* **23** (1972), 307–314.

31. A. LEONARD, *in* "Turbulent Shear Flows, II" (L. J. S. Bradbury *et al.* Eds.), pp. 67–77, Springer-Verlag, Berlin, 1980.

32. P. G. SAFFMAN, *Studies Appl. Math.* **49** (1970), 371–380.

33. R. BETCHOV, *J. Fluid Mech.* **22** (1965), 471–479.

34. H. HASIMOTO, *J. Fluid Mech.* **51** (1972), 477–485.

35. J. H. FERZIGER, *AIAA J.* **15** (1977), 1261–1267.

36. U. SCHUMANN, G. GRÖTZBACH, AND L. KLEISER, *in* "Prediction Methods for Turbulent Flows," Hemisphere, New York, 1980.

37. B. FORNBERG, *J. Comput. Phys.* **25** (1977), 1–31.

38. Y. OSHIMA AND S. ASAKA, *J. Phys. Soc. Japan* **42** (1977), 1391–1395.

39. T. FOHL AND J. S. TURNER, *Phys. Fluids* **18** (1975), 433–436.

40. A. LEONARD, *in* Lecture Notes in Physics No. 35," pp. 245–250, Springer-Verlag, New York/Berlin, 1975.

41. A. LEONARD, *in* "Lecture Notes in Physics No. 59" pp. 280–284, Springer-Verlag, New York/Berlin, 1976.

42. M. LANDAHL, private communication, 1977.

43. E. ACHENBACH, *J. Fluid Mech.* **54** (1972), 565–575.

44. A. J. CHORIN, *SIAM J. Sci. Stat. Comp.*, **1** (1980), 1–21.

45. C. REHBACH, *Rech. Aerospatiale*, No. 1977-5 (1977), 289–298; also AIAA Paper 78–111, AIAA Aerospace Science Meeting, Huntsville, Ala., Jan. 16–18, 1978.

46. J. E. HACKETT AND P. F. EVANS, *J. Aircraft* 11 (1977), 1093–1101.

47. V. R. CORSIGLIA AND K. L. ORLOFF, "Scanning Laser-Velocimeter Surveys and Analysis of Multiple Vortex Wakes of an Aircraft," NASA TM X-73,169, 1976.

48. D. L. CIFFONE AND C. LONZO, JR., "Flow Visualization of Vortex Interactions in Multiple Vortex Wakes behind Aircraft," NASA TM X-62,459, 1975.

49. M. R. BARBER, "Vortex Attenuator Flight Experiments," NASA Symp. on Wake Vortex Minimization, Washington, D. C., Feb. 25–26, 1976 (NASA SP 409).

50. F. R. Hama, *Phys. Fluids* 6 (1963), 526–533.

51. V. DEL PRETE, "Numerical Simulation of Vortex Breakdown," LBL-8503, Lawrence Berkeley Lab., Berkeley, Calif., Oct. 1978.

52. J. C. S. MENG, *J. Fluid Mech.* 84 (1978), 455–469.

53. J. P. CHRISTIANSEN, *J. Comput. Phys.* 13 (1973), 363–379.

54. G. R. BAKER, *J. Comput. Phys.* 31 (1979), 76–95.

55. R. W. HOCKNEY, S. P. GOEL, AND J. W. EASTWOOD, *J. Comput. Phys.* 14 (1974), 148–158.

56. O. BUNEMAN, *J. Comput. Phys.* 11 (1973), 250–268.

57. O. BUNEMAN, *in* "Lecture Notes in Physics, No. 35," pp. 111–115, Springer-Verlag, New York/Berlin, 1974.

58. O. BUNEMAN, *Computer Phys. Comm.* 12 (1976), 21–31.

59. B. COUËT, "Evolution of Turbulence by Three-Dimensional Numerical Particle-Vortex Tracing," Ph. D. thesis, Stanford University Institute for Plasma Research No. 793, 1979.

60. S. S. WANG, "Grid-Insensitive Computer Simulation of the Kelvin–Helmholtz Instability and Shear Flow Turbulence," Ph. D. thesis, Stanford University Institute for Plasma Research Report. No. 710, 1977.

61. O. BUNEMAN, B. COUËT, AND A. LEONARD, *J. Comput. Phys.*, in press.

62. B. COUËT AND A. LEONARD, *in* "Proceedings, 7th International Conference on Numerical Methods in Fluid Dynamics," in press.

63. J. N. NIELSEN, "Missile Aerodynamics—Past, Future," AIAA Aircraft Systems and Technology Meeting, AIAA 79–1819 (1979).

64. W. T. ASHURST, "Vortex Dynamic Calculation of Fluid Motion in a Four Stroke Piston 'Cylinder'—Planar and Axisymmetric Geometry," SAND 79–8229, Sandia Lab., Livermore, Calif., 1978.